Correlation-Enhanced Electron-Phonon Coupling: Applications of *GW* and Screened Hybrid Functional to Bismuthates, Chloronitrides, and Other High-T_c Superconductors

Z. P. Yin,* A. Kutepov, and G. Kotliar

Department of Physics and Astronomy, Rutgers University, Piscataway, New Jersey 08854, United States

(Received 26 September 2012; revised manuscript received 7 March 2013; published 30 May 2013)

We show that the electron-phonon coupling (EPC) in many materials can be significantly underestimated by the standard density-functional theory (DFT) in the local-density approximation (LDA) due to large nonlocal correlation effects. We present a simple yet efficient methodology to evaluate the realistic EPC, going beyond the LDA by using more advanced and accurate *GW* and screened-hybrid-functional DFT approaches. The corrections that we propose explain the extraordinarily high superconducting temperatures that are observed in two distinct classes of compounds—the bismuthates and the transition-metal chloronitrides—thus solving a 30-year-old puzzle. Our work calls for the critical reevaluation of the EPC of certain phonon modes in many other materials, such as cuprates and iron-based superconductors. The proposed methodology can be used to design new correlation-enhanced high-temperature superconductors and other functional materials that involve electron-phonon interaction.

DOI: 10.1103/PhysRevX.3.021011 Subject Areas: Computational Physics, Materials Science, Superconductivity

I. INTRODUCTION

The microscopic origin of superconductivity has been established in numerous classes of materials. In conventional superconductors such as elemental metals, it results from the exchange of phonons. In the copper oxides, the iron pnictides, and some organic compounds, superconductivity is connected to close proximity to a magnetic state. On the other hand, the cause of superconductivity in a large third class of high-temperature superconductors, including $Ba_{1-x}K_xBiO_3$ ($T_{c,\max} \simeq 32$ K) [1], electron-doped β-HfNCl compounds ($T_{c,\max} \simeq 25.5$ K) [2], and alkali-doped fullerides A_3C_{60} ($T_{c,\max}$ up to 40 K) [3], is still mysterious. They have been referred to as the "other high-temperature superconductors" [4,5] because neither spin nor phonon seems to be responsible for their high superconducting temperatures.

Since they are apparently diamagnetic (and thus the spin degree of freedom seems irrelevant), two charge-mediated pairing mechanisms have been proposed (and ruled out) for the bismuthates: the "negative U" scenario [6,7] and strong coupling to an O-breathing phonon mode [8,9]. The first scenario involves the tendency of Bi atoms to avoid the Bi^{4+} state while preferring the Bi^{3+} and Bi^{5+} charge states, thus generating an attractive local negative U pairing center. However, first-principles calculations have so far ruled out the negative U mechanism [10,11]. Regarding the electron-phonon mechanism, previous approaches to the *ab initio* evaluation of the electron-phonon coupling (EPC) were based on the density-functional theory (DFT) and linear-response theory (LRT) [12] in the local-density approximation (LDA) or generalized-gradient approximation (GGA). The EPC calculated by this standard DFT LDA or GGA approach is insufficient to account for the high T_c in both $Ba_{1-x}K_xBiO_3$ [13] and the electron-doped transition-metal chloronitrides [14,15] within the Migdal-Eliashberg theory, which seems to rule out the phonon mechanism.

However, to rule out the phonon mechanism, the EPC has to be evaluated reliably. It is well known that the standard DFT LDA or GGA approach fails to describe well the electronic structure of strongly correlated materials. This shortcoming of the LDA and GGA raises the question of whether the EPC is properly treated by the standard DFT LDA or GGA approach for the other high-temperature superconductors [4,5] and other correlated materials in general. Despite the answer to this question, a reliable evaluation of electron-phonon-interaction (EPI) strength for real materials is of fundamental importance for both understanding the underlying physics and designing novel functional materials. (The EPC for metallic materials is the average of EPI matrix elements on the Fermi surface.) The EPI or EPC plays an important role not only in conventional superconductivity but also in electronic transport, electronic-heat capacity, etc. Even in the cuprate superconductors, there is evidence [16–19] (see also Ref. [20] for a review) that the EPC is strong and may play an important role in the unconventional superconductivity [18].

The EPC for materials can be estimated by both experimental techniques and theoretical methods. Experimentally, its strength can be estimated by means of neutron scattering [21], Raman scattering [22], tunneling [23], and photoemission [18]. However, these experiments are usually limited to be able to estimate the EPC strength for only a few phonon modes [18,22,24,25]. Theoretically, first-principles

*yinzping@physics.rutgers.edu

calculations based on density-functional theory and the linear-response technique, on the other hand, can provide a complete evaluation of the EPI, including all phonon modes, and is widely used for calculating lattice dynamical properties and the EPCs of solids. For example, the EPCs evaluated by this approach with the LDA or GGA are strong enough to account for the rather high-temperature superconductivity in conventional superconductors such as elemental lithium ($T_c \sim 20$ K) [26], yttrium ($T_c \sim 20$ K) [27], calcium ($T_c \sim 25$ K) [28], and the binary compound MgB_2 ($T_c \sim 40$ K) [29]. This recorded success of the LDA and/or GGA linear-response calculations for conventional superconductors gives rise to the puzzles about the mechanism of superconductivity in the other high-temperature superconductors, including the bismuthates and the transition-metal chloronitrides, as mentioned above.

In this paper, we show that these other high-temperature superconductors are strongly coupled superconductors where the couplings of the electrons to the lattice vibrations are strongly enhanced by correlation effects, which requires treatments of electron-electron interaction beyond the LDA or GGA. Once the EPC is properly evaluated, it is strong enough to account for their high-temperature superconductivity. Our view is supported by various experiments that show strong EPCs for certain phonon modes of these superconductors [30–33].

The key is to overcome the overscreening problem of the LDA or GGA and achieve a simultaneous faithful description of the ground-state electronic structures and lattice dynamical properties. We will show that an appropriate screened hybrid functional and quasiparticle GW (QPGW) method provide an accurate description of the normal-state electronic structures, and can be combined with the linear-response approach to accurately determine lattice dynamical properties and the EPC of these materials. The problem is that the GW method and the screened-hybrid-functional approach are very computationally demanding; combining them directly into the linear-response approach poses a serious challenge to modern technology. It is, therefore, desirable to have a simplified method to estimate the EPC strength to a reasonable accuracy.

To this end, we propose such a method, based on LDA or GGA linear-response calculations and a few GW and/or screened-hybrid-functional supercell calculations. The latter calculations are used to replace the most important electron-phonon matrix elements in the LDA or GGA linear-response calculations to obtain an improved evaluation of the EPC. We apply our method to the (Ba, K)BiO_3 and electron-doped HfNCl high-temperature superconductors and find that the EPCs computed by our method are significantly enhanced, in comparison to the values predicted by LDA or GGA linear-response calculations, and are strong enough to account for the experimental T_c in these materials within the standard Migdal-Eliashberg theory. Therefore, the puzzling high-temperature superconductivity in this class of superconductors is naturally explained. In addition, our method explains the material and doping dependence of T_c in these superconductors and related compounds. Our method can also be used to design new high-temperature superconductors and other EPI- or EPC-related functional materials.

This paper is organized as follows: We first clarify two sources of electronic correlations, starting from the LDA or GGA, and their impacts on lattice dynamic properties (Sec. II). A general understanding of the EPC and our method to estimate the EPC, combining LDA or GGA linear-response calculations and GW or screened-hybrid-supercell calculations, is presented in Sec. III. Section IV summarizes our computational details. The electronic structures, selected important phonon frequencies, and EPCs calculated by the LDA or GGA functional, the screened hybrid functional, and the QPGW approach are presented for (Ba, K)BiO_3 materials in Sec. V and electron-doped HfNCl/ZrNCl materials in Sec. VI. A short summary is provided in Sec. VII, followed by discussions. The paper is concluded in Sec. VIII.

II. ELECTRONIC CORRELATION AND ITS IMPACT ON LATTICE DYNAMIC PROPERTIES

The frequency- and momentum-resolved Green's function $G(\omega, k)$ can be written as $G(\omega, k) = 1/[\omega - H(k)_{\text{mean field}} - \Sigma(\omega, k)]$, where $H(k)_{\text{mean field}}$ is some mean-field Hamiltonian and $\Sigma(\omega, k)$ is the self-energy correction induced by correlation effects. Naturally, $\Sigma(\omega, k)$ depends on the choice of the mean-field method, hence the term "correlation." Chemists usually use the Hartree-Fock method as the mean field, whereas many physicists prefer the LDA or GGA within the DFT framework as the starting point. Here, we adopt the physicists' choice, i.e., $H(k)_{\text{mean field}} = H(k)_{\text{DFT LDA or GGA}}$, and define correlation with respect to deviations from the DFT LDA or GGA. With this choice, the degree of correlation is quantified by $\Sigma(\omega, k)$.

When $\Sigma(\omega, k)$ is negligible, the correlation is weak, and static mean-field theory such as the DFT LDA or GGA is reasonably accurate, for example, for Cu and Au. However, when $\Sigma(\omega, k)$ is large, the correlation is strong and has to be treated by approaches beyond the DFT LDA or GGA. There are different cases where the correlation can be taken into account by different methods.

If $\Sigma(\omega, k)$ is dominated by the frequency dependence, the correlation is mainly local and is caused by the degeneracy error of the LDA or GGA [34]. This local correlation is addressed by dynamical mean-field theory (DMFT) combined with the DFT LDA or GGA [35,36].

On the other hand, if $\Sigma(\omega, k)$ mostly has momentum dependence, the correlation is mainly nonlocal and is rooted in the semilocal nature of the LDA or GGA, which neglects the long-range exchange interaction. This nonlocal correlation can be accounted for by including

long-range exchange interactions. The *GW* method is able to determine the range of the exchange potential self-consistently and is suited to deal with the nonlocal correlation. The disadvantage is that *GW* calculations are often very computationally demanding. The most economical way to incorporate the long-range exchange interaction (nonlocal correlation) is by replacing the LDA or GGA functional by a screened hybrid functional [37], such as the Heyd-Scuseria-Ernzerhof hybrid functional (HSE06) [38], which increases the spatial nonlocality of the exchange potential relative to the LDA or GGA. The downside of the screened-hybrid-functional approach is that it contains an empirical mixing parameter α (0.25 for HSE06) of the Hartree-Fock potential and a screening parameter μ (0.2 for HSE06) to adjust the range of the spatial nonlocality and to avoid the spin-density wave instability in the Hartree-Fock method[39,40]. This drawback has already been faced with a lot of criticism of its less *ab initio* nature in comparison to the LDA or GGA functional. To avoid this problem, we fixed $\alpha = 0.25$ for all the screened-hybrid-functional calculations, and we compare the screened-hybrid-functional results with quasiparticle *GW* results to determine the μ parameter. Therefore, we have no free parameter in our screened-hybrid-functional calculations, and our approach preserves the most valuable predictive power of the *ab initio* method. It was shown that HSE06 shares the same feature as QP*GW* in accounting for the electronic structures and lattice dynamical properties of the parent $BaBiO_3$ compound [41,42].

Finally, if both frequency and momentum dependence are important in $\Sigma(\omega, k)$, there are strong local and nonlocal correlations. To treat the local and nonlocal correlations simultaneously, we need to combine the above methods, such as *GW* + DMFT [43,44] and screened hybrid DFT + DMFT [45].

It has been established that the local correlation, as seen in many partially filled *d*- and *f*-shell materials, often has strong effects on lattice dynamical properties. For example, DMFT greatly improves the LDA on the phonon spectra in Pu [46] and in the transition-metal oxides MnO and NiO [47]. In the doped cuprate superconductors, the experimental width of the half-breathing phonon is about an order of magnitude larger than that predicted by LDA calculations [48].

In parallel, the screened hybrid functional has been shown to be an improvement over the LDA or GGA for the phonon spectra of many materials, including semiconductors [49–51], oxides [52], and molecules [53]. Note that the *GW* method and the (screened) hybrid functional are usually used to correct the underestimated LDA or GGA band gaps of some insulators and semiconductors. These approaches are generally believed to have little effect on, or perform worse than, the LDA or GGA for metallic systems [40,54]. The impact of nonlocal correlation on the lattice dynamical properties and on the EPC of metallic materials has not been carefully studied.

In this paper, we will show that the nonlocal correlation can also have substantial impacts on the lattice dynamical properties of metallic materials where the LDA or GGA strongly overscreens the electronic states, such as conducting materials in the vicinity of a metal-insulator transition (i.e., the parent compound is an insulator, while the doped compound becomes metallic upon sufficient doping). We find that the screened-hybrid-functional approach, when adjusted to match with the QP*GW* results, is able to reproduce the experimental electronic structures and phonon frequencies of both the other high-temperature superconductors—the bismuthates and the transition-metal chloronitrides for which LDA or GGA calculations show large discrepancies with experimental observations and a conventional high-temperature superconductor MgB_2, for which LDA or GGA calculations show fewer discrepancies with experimental observations.

III. EVALUATION OF ELECTRON-PHONON COUPLING

We now present our approach to evaluate the electron-phonon coupling. The EPC strength λ can by written as [55] (the band index is omitted for simplicity)

$$\lambda = \frac{2}{N(\varepsilon_F) N_q} \sum_{k,q,\nu} |M^{\nu}_{k,k+q}|^2 \delta(\varepsilon_k - \varepsilon_F) \delta(\varepsilon_{k+q} - \varepsilon_F) / \omega_{q\nu}, \tag{1}$$

where N_q is the number of q points, $N(\varepsilon_F)$ is the total density of states per spin at the Fermi level ε_F, $\omega_{q,\nu}$ is the phonon frequency of branch ν with wave vector q, and $M^{\nu}_{k,k+q}$ are the electron-phonon matrix elements given by

$$M^{\nu}_{k,k+q} = \sum_j \left(\frac{\hbar^2}{2 M_j \omega_{q\nu}} \right)^{1/2} \epsilon^{\nu}_{q,j} \cdot \langle k+q | \delta V / \delta u^{\nu}_{q,j} | k \rangle, \tag{2}$$

where j runs over the atoms in the unit cell and $\delta V / \delta u^{\nu}_{q,j}$ is the partial derivative of the total Kohn-Sham potential energy with respect to a given phonon displacement u^{ν}_q of the jth atom. For optical vibration modes, with a wave vector q commensurate with the lattice, the electron-phonon matrix element can be inferred from the shifts of the energy bands in a supercell calculation (frozen phonons), which we denote as the reduced electron-phonon matrix element (REPME) $D^{\nu}_{k,q}$. For states on the Fermi surface, the electron-phonon matrix elements can be read directly from the splitting of the energy bands that result from the phonon displacements.

As we shall show later, the modifications in the more advanced approaches of the Fermi surface, the density of states $N(\varepsilon)$ and the corresponding phonon frequencies $\omega_{q,\nu}$, compared to the LDA or GGA, are significantly smaller than those of the electron-phonon matrix elements. Hence, the electron-phonon matrix elements are the dominating factor, causing the realistic λ to be different from

the LDA or GGA value. As a result, the realistic EPC λ can be estimated from a LRT LDA or GGA calculation by rescaling the LDA or GGA REPMEs to the actual values given by more advanced approaches while keeping the integral over k and q of Eq. (1) at the LDA or GGA level. Here, the more advanced approach should be able to accurately reproduce the ground-state properties (compared to LDA or GGA). In practice, a good estimation is achieved by using both an advanced approach and a LDA or GGA to evaluate the REPMEs for all the strongly coupled phonon modes (which can be seen in the LDA or GGA linear-response calculation) at special points in the Brillouin zone:

$$\lambda_A = \sum_\nu \lambda_{A\nu} \simeq \sum_\nu \lambda_{L\nu} \langle |D_A^\nu|^2 \rangle / \langle |D_L^\nu|^2 \rangle, \tag{3}$$

where we denote the advanced approach (such as the GW and screened-hybrid-functional approaches) as A and the LDA or GGA as L. If the enhancements in the REPMEs of all the strongly coupled branches are of comparable magnitude, we can estimate λ_A by

$$\lambda_A \simeq \lambda_L \langle |D_A^\nu|^2 \rangle / \langle |D_L^\nu|^2 \rangle. \tag{4}$$

We note that the accuracy of estimating the realistic EPC using the above method can be improved by including more phonon modes when more computing resources are available. Eventually, to achieve a more accurate evaluation of the realistic EPC, the linear-response technique should be implemented into the GW and/or the screened-hybrid-functional DFT.

IV. COMPUTATIONAL DETAILS

A. Method

The electronic structures are calculated using both the VASP [56] code with GGA in the Perdew-Burke-Ernzerhof (PBE) form [57] and HSE06 [38] exchange-correlation functionals and the WIEN2k [58] code with a GGA (PBE) [57] exchange-correlation functional. Linear-response calculations are carried out using the LMTART [12,59] code with the ideal cubic structures (i.e., without distortions). The crystal structures are taken from Ref. [60] for $BaBiO_3$ and from Ref. [61] for $BaPbO_3$. For VASP calculations, the projector-augmented-wave PBE pseudopotential is used in both DFT GGA and DFT HSE calculations. The energy cutoff for the wave function is 400 eV. The results of the GGA calculations from VASP are double checked with results from WIEN2k with a GGA (PBE) exchange-correlation functional. In linear-response calculations, a 32^3 k mesh is used to converge the electron charge density. The electron-phonon-coupling constant is obtained with an 8^3 q mesh with 35 independent q points in the irreducible Brillouin zone. We use virtual crystal approximation to simulate the doping effect in the linear-response calculations.

For GW calculations, we use the self-consistent quasiparticle GW (scQPGW) as implemented in VASP. To ensure good convergence of the scQPGW calculations, we use an energy cutoff of 400 meV, 480 bands, and a $6 \times 6 \times 6$ k mesh for the ten-atom/cell (Ba, K)BiO_3 and of 240 bands and a $12 \times 12 \times 4$ k mesh for the six-atom/cell Hf/ZrNCl compounds.

B. Frozen-phonon calculations

For the frozen-phonon calculations, we create supercells that are adaptive to the momentum q of the phonon mode. For example, to calculate the oxygen-breathing frequency at the X, M, and R points in bismuthates, we create $2 \times 1 \times 1$, $2 \times 2 \times 1$, and $2 \times 2 \times 2$ supercells of the simple cubic unit cell, respectively. Upon the atomic displacement u of a phonon mode with wave vector q, the phonon frequency is extracted as $\omega = [E''(u)|_{u=0}/M_{\text{eff}}]^{1/2}$ in the harmonic approximation, where M_{eff} is the effective mass, and $E(u)$ is the total energy as a function of the atomic displacement u in the DFT frozen-phonon calculation. For instance, the effective mass M_{eff} is 6 times the oxygen atomic mass in calculating the oxygen-breathing frequency at the R point.

C. Estimation of $\omega_{\log}$

While $\omega_{\log}$ usually decreases with increasing λ, there is not a simple relation between them. Following a discussion in Ref. [33], we estimate the HSE06 value $\omega_{\log,H}$ in optimal hole-doped $BaBiO_3$ (and other compounds considered in this article) from the corresponding LDA value $\omega_{\log,L} \simeq 550$ K [13] via an empirical relation as $\omega_{\log,H} \simeq \omega_{\log,L}(1+\lambda_L)^{1/2}/(1+\lambda_H)^{1/2} \simeq 450$ K, which is in good agreement with the value about 450 K that was extracted from experiments [30,62]. The good agreement of the $\omega_{\log}$ in optimal hole-doped $BaBiO_3$ between the estimated HSE06 value and the experimental value suggests that (a) the above relation is a reasonable approximation and that (b) the HSE06 λ_H is close to the realistic EPC in this material, which further supports our view that HSE06 is appropriate for estimating the EPC in $BaBiO_3$-related materials.

D. Evaluating the Coulomb pseudopotential

To estimate the Coulomb pseudopotential μ^*, we implement the methodology of Ref. [63] in our codes [64,65], which combine the LDA and GW methods in a linearized augmented plane-wave basis set. μ^* is given by the formula

$$\mu^* = \frac{\mu}{1 + \mu \ln \frac{\varepsilon_F}{\omega_D}}, \tag{5}$$

where ε_F is the Fermi energy and ω_D the Debye energy, and the dimensionless parameter μ is calculated as the following average over the Fermi surface

$$\mu = N(\varepsilon_F)\frac{\sum_{\mathbf{k}\mathbf{k}'}\sum_{\lambda\lambda'} W_{\mathbf{k}\lambda;\mathbf{k}'\lambda'}\delta(\varepsilon_{\mathbf{k}\lambda}-\varepsilon_F)\delta(\varepsilon_{\mathbf{k}'\lambda'}-\varepsilon_F)}{\sum_{\mathbf{k}\mathbf{k}'}\sum_{\lambda\lambda'}\delta(\varepsilon_{\mathbf{k}\lambda}-\varepsilon_F)\delta(\varepsilon_{\mathbf{k}'\lambda'}-\varepsilon_F)}, \quad (6)$$

where $N(\varepsilon_F)$ is the density of states at the Fermi level per spin, $\varepsilon_{\mathbf{k}\lambda}$ is the Kohn-Sham eigenvalue of the λth band at a wave vector $\mathbf{k}$, and matrix elements of the screened Coulomb interaction in a basis of the LDA eigenstates are calculated as the following:

$$W_{\mathbf{k}\lambda;\mathbf{k}'\lambda'} = \langle \mathbf{k}'\lambda'\uparrow, -\mathbf{k}'\lambda'\downarrow | W | \mathbf{k}\lambda\uparrow, -\mathbf{k}\lambda\downarrow\rangle. \quad (7)$$

The resulting μ^* for the ideal $BaBiO_3$, $BaPbO_3$, and $LaPbO_3$ compounds are 0.104, 0.117, and 0.119, respectively.

The difference between our work and Ref. [63] is that we use finite-temperature formalism and approximate the δ function with the imaginary part of the LDA Matsubara Green's function

$$\delta(\varepsilon_{\mathbf{k}\lambda}-\varepsilon_F) \approx \mathrm{Im}\frac{1}{i\omega_0+\varepsilon_F-\varepsilon_{\mathbf{k}\lambda}}, \quad (8)$$

where ω_0 is the smallest positive Matsubara frequency. The expression (8) becomes exact in the limit of zero temperature. Technically, we perform the following steps. First, we calculate a LDA one-electron spectrum and corresponding wave functions. It provides us with a LDA Green's function. Then, we evaluate the LDA polarizability $P_{\mathrm{LDA}} = G_{\mathrm{LDA}}G_{\mathrm{LDA}}$. The third step is to calculate the screened interaction $W = V + VP_{\mathrm{LDA}}W$, where V is the bare Coulomb interaction. After the third step, we are able to get the Coulomb pseudopotential parameter.

V. BISMUTHATES

We first apply our method to the bismuthate $Ba_{1-x}K_xBiO_3$, which was found to superconduct below 32 K in 1988 [1].

A. Crystal structure

The optimal doped $BaBiO_3$ (and $BaPbO_3$) crystallize in the simple cubic perovskite structure, as is shown in Fig. 1, whereas the parent compounds (without doping) display certain distortions from the ideal perovskite structure [60,61]. There are two types of distortions: One is the oxygen-breathing distortion along nearest-neighbor M-O bonds (M = Bi and Pb), as is shown in Fig. 1(a). The other one is the oxygen-tilting distortion perpendicular to the nearest-neighbor M-O bonds (not shown). The oxygen-breathing vibration was found to show strong EPC [13,66,67].

B. LDA linear-response calculation

We first reproduce the LRT LDA calculations of Ref. [13] and show the results in Figs. 1(d) and 1(e). We find that the oxygen-breathing or stretching mode around the R point [Fig. 1(a)] and around the M point [Fig. 1(b)]

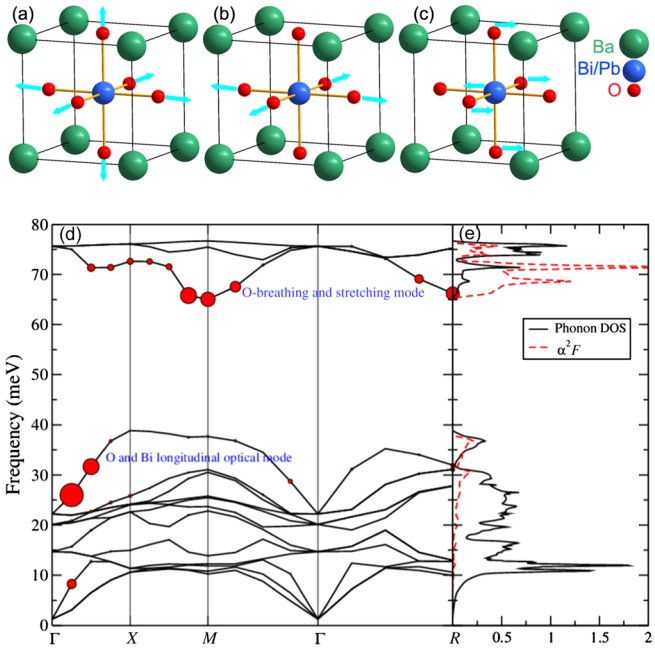

FIG. 1. Top panel: Crystal structure of $BaBiO_3$ and $BaPbO_3$. The arrows show (a) the oxygen breathing, (b) the oxygen stretching, and (c) oxygen and bismuth longitudinal optical vibration modes (the ferroelectric longitudinal optical mode). Bottom panel: (d) Phonon spectra and mode- and momentum q-dependent electron-phonon-coupling strength $\lambda_{q,\nu}$ (its value is proportional to the size of the circle at each q point) and (e) the corresponding phonon density of states and the Eliashberg function $\alpha^2F(\omega)$ of 0.4 hole-doped $BaBiO_3$.

dominates the contributions to the total λ, as is evident from the mode- and momentum-dependent EPC $\lambda_{q,\nu}$ shown in Fig. 1(d) and the Eliashberg function $\alpha^2F(\omega)$ shown in Fig. 1(e). In addition, we find at small q a longitudinal optical mode (the so-called ferroelectric mode) depicted in Fig. 1(c) that also has a substantial EPC. These findings are in good agreement with previous observations [13,66,67]. On the contrary, acoustic phonon modes have very little contribution to the total EPC. With these findings, we argue that it is appropriate to use Eq. (3) to estimate the realistic EPC strength λ_A from LRT LDA calculations in (Ba, K)BiO_3.

C. Density of states

It has been noted [13] that the LDA suffers large discrepancies in describing the ground-state properties of the parent compounds and some lattice dynamical properties of the metallic doped compounds, in comparison with experiments. Recently, it was shown that a screened hybrid functional such as HSE06 [38] largely removes the overscreening of the LDA or GGA in the insulating (parent and lightly hole-doped) $BaBiO_3$ compounds and describes many of their physical properties in excellent agreement with experiments [41,42]. It is not clear, however, if the

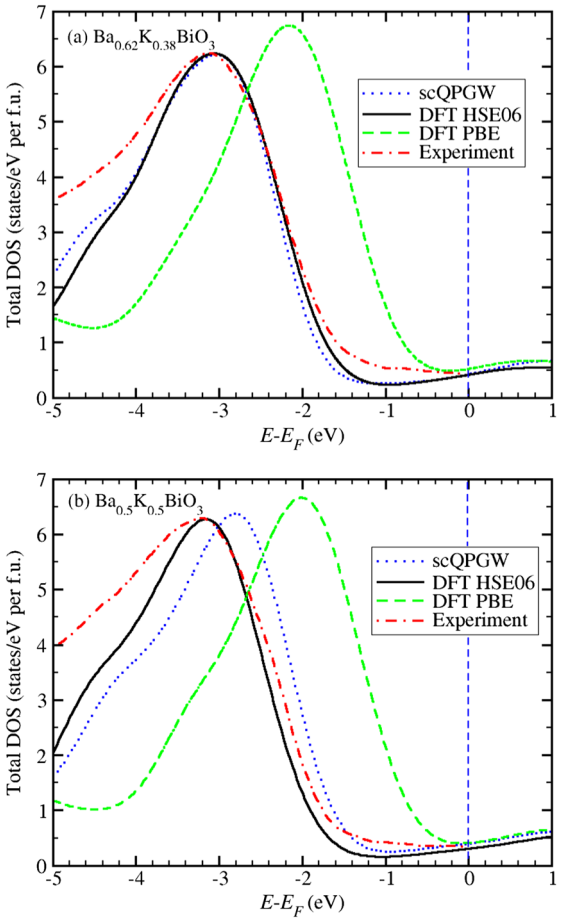

FIG. 2. Densities of states of $Ba_{0.62}K_{0.38}BiO_3$ and $Ba_{0.5}K_{0.5}BiO_3$. (a) The DOS of $Ba_{0.62}K_{0.38}BiO_3$, calculated using the PBE functional, the HSE06 screened hybrid functional, and the self-consistent quasiparticle GW, where doping is approximated with the rigid band approximation. (b) The DOS of $Ba_{0.5}K_{0.5}BiO_3$, calculated using the PBE functional, the HSE06 screened hybrid functional, and the self-consistent quasiparticle GW. Here, the doping is simulated with a $2 \times 2 \times 2$ supercell by substituting half of the Ba atoms with K atoms. The experimental data are the ultraviolet photoemission spectra for (a) $Ba_{0.62}K_{0.38}BiO_3$ and (b) $Ba_{0.52}K_{0.48}BiO_3$, taken from Ref. [68].

screened hybrid functional also provides an improved description of the metallic hole-doped $BaBiO_3$ compounds.

Here, we show in Fig. 2(a) the calculated density of states (DOS) of an optimal doped compound $Ba_{0.62}K_{0.38}BiO_3$, using both the PBE functional and the HSE06 functional in the DFT framework, and the self-consistent quasiparticle GW method, based on virtual crystal approximation (VCA) and rigid band approximation (RBA), and we compare them with the experimental ultraviolet photoemission spectra (UPS) [68] of $Ba_{0.62}K_{0.38}BiO_3$. We note that the difference between the RBA and the VCA is small with the PBE functional; therefore, only the RBA result is displayed in Fig. 2(a). The HSE06 DOS is almost the same as the scQPGW DOS, and both of them have an overall good agreement with the experimental UPS: In particular, they share roughly the same peak of the oxygen $2p$ states centered at about -3.1 eV. In contrast, the DOS from the PBE calculation has a peak centered at about -2.2 eV, 0.9 eV away from the experimental position.

In Fig. 2(b), we show the DOS for $Ba_{0.5}K_{0.5}BiO_3$, calculated with PBE and HSE06 functionals, and the scQPGW method. Instead of using the VCA or the RBA, we use a $2 \times 2 \times 2$ supercell and replace half of the Ba atoms with K atoms to minimize errors induced by such approximations. We compare the results with the experimental UPS data for $Ba_{0.52}K_{0.48}BiO_3$ from Ref. [68]. Again, we find a very good agreement between the HSE06 calculated DOS and experimental spectra. The peak position of the scQPGW DOS is 0.4 eV off the experimental one, whereas the peak position of the PBE DOS is 1.2 eV off the experimental one.

Therefore, both the scQPGW method and the HSE06 screened hybrid functional provide a significantly improved description of the electronic structures of the metallic (Ba, K)BiO_3 compounds compared to the GGA results, in strong contrast to the common belief that the GW and hybrid functionals are worse than the LDA or GGA for metals.

D. Phonon frequencies

It is not currently feasible to compute the phonon frequencies using the scQPGW method. Here, we provide evidence that the HSE06 also improves the estimation of phonon-related quantities over the LDA or GGA for the metallic (Ba, K)BiO_3 compounds. The scQPGW phonon frequencies are expected to be similar to the HSE06 results. We show in Table I the phonon frequencies of the oxygen-breathing or stretching mode at the X, M, and R points and the so-called ferroelectric longitudinal optical phonon mode (see Fig. 1) at the Γ and X points in $BaKBi_2O_6$ (a realistic K doping into $BaBiO_3$) computed using the frozen-phonon method with both the GGA and the HSE06. We also display in Table I the phonon frequencies computed by the DFT GGA and the LRT LDA with the VCA for $Ba_{0.6}K_{0.4}BiO_3$ and $Ba_{0.5}K_{0.5}BiO_3$ and compared with available experiments from Ref. [69] for $Ba_{0.6}K_{0.4}BiO_3$ and Ref. [33] for $Ba_{0.48}K_{0.52}BiO_3$. For the oxygen-breathing mode at the M and R points, we find that the HSE06 frequencies are in very good agreement with the experimental data, whereas the GGA overestimates the experimental frequencies by about 10%. The HSE06 improves the GGA on the oxygen-breathing frequency at the X point, where the HSE06 (GGA) overestimates the experimental value by 9% (21%). For the ferroelectric longitudinal optical mode, the phonon frequency at the X point is similar in the HSE06 and the GGA, as is expected from the small $\lambda_{q,\nu}$ shown in Fig. 1. However, at the Γ point, the HSE06 phonon frequency of this mode (18.1 meV) is considerably smaller than the GGA value

TABLE I. Phonon frequencies of the important longitudinal optical phonon modes at high symmetry points in $BaKBi_2O_6$, calculated by supercell frozen-phonon calculations in the DFT GGA and DFT HSE06 framework. For comparison, the corresponding phonon frequencies from the LRT LDA calculations for $Ba_{0.6}K_{0.4}BiO_3$ and $Ba_{0.5}K_{0.5}BiO_3$ using the VCA, as well as from experimental measurements (experiment 1 from Ref. [69] and experiment 2 from Ref. [33]), are also displayed.

Doping method	Q	DFT GGA K substitution	DFT HSE06 K substitution	DFT GGA VCA	LRT LDA VCA	LRT LDA VCA	Experiment 1 K substitution	Experiment 2 K substitution
Mode or Doping x		0.5	0.5	0.5	0.5	0.4	0.4	0.52
Breathing	R	68.4	**61.2**	72.3	75.1	68.6	**62**	
	M	64.7	**59.0**	64.3	68.8	67.9	**60**	
	X	66.6	**60.1**	71.0	74.2	75.9	**55**	**55**
Ferroelectric	Γ	22.7	**18.1**	22.9	23.8	23.6	25	**18**
	X	37.2	**38.1**	38.6	39.7	39.7	**36**	**35**

(22.7 meV) because of the enhanced $\lambda_{q,\nu}$ and is in good agreement with the experimental observation (approximately 18 meV) [33].

E. Band structures and reduced electron-phonon matrix elements

As an example, we show in Fig. 3 the band structures of $BaBiO_3$ with and without the oxygen-breathing displacement [see Fig. 1(a)] to illustrate the huge differences in the REPME of the oxygen-breathing mode at the R point computed by the GGA and the HSE06. The band splittings indicated by the arrows in Fig. 3 are about 1.17 eV for the DFT HSE06 and 0.67 eV for the DFT GGA, upon a displacement of 0.044 Å, resulting in REPMEs of about 13.3 and 7.6 eV/Å, respectively. We also compute this splitting using the scQPGW under the same displacement. The corresponding value is 1.10 eV, resulting in a REPME of about 12.5 eV/Å. The scQPGW results confirm again that the HSE06 is applicable to the metallic (Ba, K)BiO_3 compounds. The above results indicate that the EPC strength for this mode is strongly enhanced by about a factor of 3 in the more accurate HSE06 and scQPGW treatments, in comparison to the LDA value. Notice that the material remains metallic with the oxygen-breathing distortion; therefore, the enhanced REPME in the HSE06 and scQPGW approaches, compared to the LDA value, is not merely a band-gap problem of the LDA.

We also compute the REPME of the oxygen-breathing mode at the R point (see Fig. 4) in $BaKBi_2O_6$ and find it to be about 13.7, 11.0, and 7.8 eV/Å in the scQPGW, the HSE06, and the GGA, respectively. Notice again that the material remains metallic with the oxygen-breathing distortion. Therefore, even in the overdoped $Ba_{0.5}K_{0.5}BiO_3$ compound, the EPC is strongly enhanced in the scQPGW (HSE06), about a factor of 3 (2) of the LDA or GGA value, confirming that the effect of doping on the REPME is relatively weak. Hence, while the LDA or GGA quantitative overestimation of the phonon frequencies is less severe than its underestimation of the REPME, they are consistent manifestations of the overscreening problem of the LDA or GGA, and calculations with the HSE06 functional bring both quantities in closer agreement with experiments.

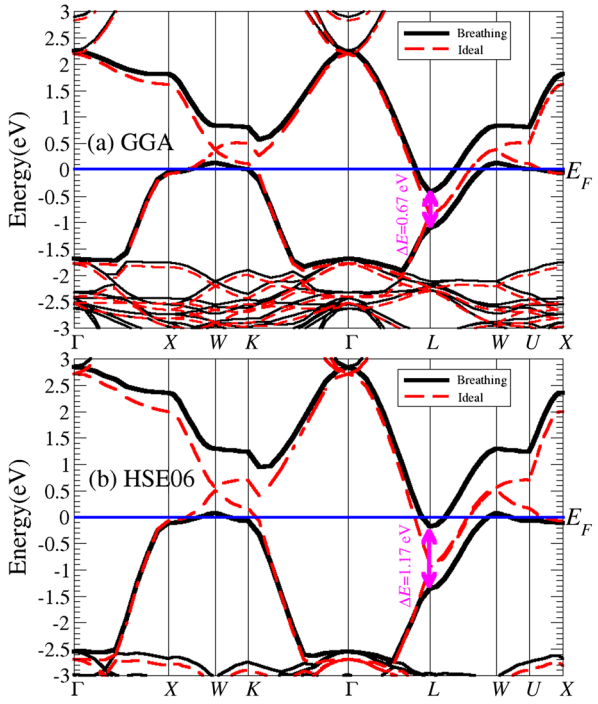

FIG. 3. Illustration of the big REPME of the oxygen-breathing mode at the R point in $BaBiO_3$. The band structures of $BaBiO_3$ with and without the oxygen-breathing displacement are calculated by DFT using both the (a) GGA and (b) HSE06 hybrid functionals. We plot the band structure in the Brillouin zone of the fcc unit cell, corresponding to a $2 \times 2 \times 2$ supercell of the simple cubic unit cell due to the oxygen-breathing distortion. The displacement of each oxygen is about 0.044 Å in the calculations. The band splittings indicated by the arrows are about 1.17 eV for the DFT HSE06 and 0.67 eV for the DFT GGA, resulting in REPMEs of about 13.3 and 7.6 eV/Å, respectively. The corresponding scQPGW values are 1.10 eV and 12.5 eV/Å, respectively. Note that the material remains metallic with the oxygen-breathing distortion.

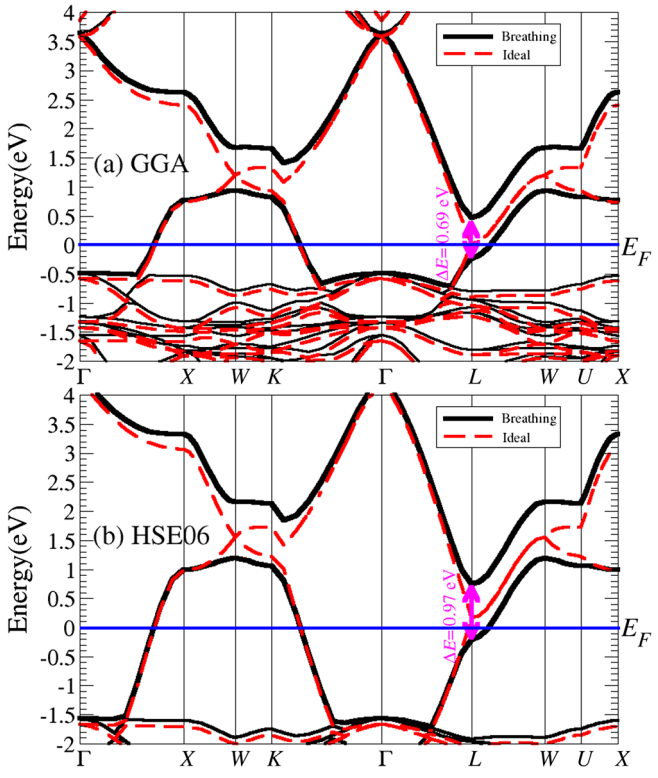

FIG. 4. Illustration of the big REPME of the oxygen-breathing mode at R in $BaKBi_2O_6$. The band structures of $BaKBi_2O_6$ with and without oxygen-breathing displacement are calculated by DFT using both the (a) GGA and (b) HSE06 hybrid functionals. We plot the band structure in the Brillouin zone of the fcc unit cell, corresponding to a $2 \times 2 \times 2$ supercell of the simple cubic unit cell, where half of the Ba atoms are replaced by K atoms. The displacement of each oxygen is about 0.044 Å in the calculations. The band splittings that are indicated by the arrows are about 0.97 eV for the DFT HSE06 and 0.69 eV for the DFT GGA, resulting in REPMEs of about 11.0 and 7.8 eV/Å, respectively. The corresponding scQPGW values are 1.21 eV and 13.7 eV/Å, respectively. Note that the material remains metallic with the oxygen-breathing distortion.

F. Realistic electron-phonon coupling and T_c

To estimate the realistic EPC, we compute the REPMEs of the three most important phonon modes, as suggested by LDA linear-response calculations. These phonon modes are depicted in Figs. 1(a)–1(c). The REPMEs of the oxygen-breathing mode with a q vector corresponding to the R point [Fig. 1(a)] have been discussed above, about 13.3, 12.5, and 7.6 eV/Å in the HSE06, scQPGW, and GGA calculations, respectively. Since the scQPGW has more or less the same results as the HSE06, we use only the HSE06 and the GGA to calculate the REPMEs for the other two phonon modes [Figs. 1(b) and 1(c)], whose values are about 8.9 and 5.7 eV/Å in the HSE06 but only 5.1 and 3.4 eV/Å in the GGA, respectively. For all three of the important phonon modes, we have $|D_H^\nu|^2/|D_L^\nu|^2 \simeq 3.0$. Based on the LRT LDA calculated EPC $\lambda_L \simeq 0.33$, we estimate the realistic electron-phonon coupling $\lambda_H \simeq 3.0\lambda_L \simeq 1.0$ for optimal hole-doped $BaBiO_3$.

At low doping, the EPC is strong enough to drive the material to a polaronic state[41], whereas for optimal doped $BaBiO_3$ (e.g., $Ba_{0.6}K_{0.4}BiO_3$), we expect that the Migdal-Eliashberg theory is valid in this region. Using the modified McMillan equation

$$T_c = \frac{\omega_{\log}}{1.20} \exp\left(-\frac{1.04(1+\lambda)}{\lambda - \mu^*(1+0.62\lambda)}\right) \quad (9)$$

with estimated $\omega_{\log} \simeq 450$ K (see Sec. IV C) and $\lambda = 1.0$, T_c is estimated to be 31 K with $\mu^* = 0.1$, which is the conventionally nominated value and is consistent with the value obtained by our first-principles calculations, as is detailed in Sec. IV D. As a result, the strong EPC strength $\lambda \simeq 1.0$ is enough to explain the high $T_c \simeq 32$ K in K-doped $BaBiO_3$ in the framework of a novel correlation-enhanced phonon-mediated mechanism.

G. Material and doping dependence of T_c

1. $BaPbO_3$

We note that the previous reasoning can also be used to estimate the EPC in one compound from another isostructural compound by comparing their REPMEs, provided that they have a similar band structure around the Fermi level when optimally doped.

We also carried out LRT LDA calculations in $Ba_{1-x}La_xPbO_3$ based on virtual crystal approximation. We find a strong doping-dependent λ_L, which is very small at small La doping and reaches a maximum value of 0.58 at $x = 0.7$. The EPC in optimal doped (Ba, La)PbO_3 is thus estimated to be about 0.58 (LDA) and 0.72 (HSE06). Our calculation suggests superconductivity with T_c up to 18 K in an optimal doped (Ba, La)PbO_3 compound (see Table VI). Experimentally, 11 K superconductivity was found in a $Ba_{1-x}La_xPbO_3$ multiphase compound synthesized at high pressure, but the crystal structure of the superconducting phase was not identified [70]. It would be very interesting to synthesize a high-quality single-crystal $Ba_{1-x}La_xPbO_3$ compound in the perovskite structure and test our theory.

2. $Ba_{n+1}Bi_nO_{3n+1}$

Our work sheds light on the mystery of the dimensionality dependence of T_c in $BaBiO_3$-related materials. In heavy fermion materials, low dimensionality enhances superconductivity relative to their three-dimensional versions [71]. On the other hand, in $BaBiO_3$-related materials, layering, as in the synthesis of $Ba_{n+1}Bi_nO_{3n+1}$ ($n = 1, 2, 3, \ldots$), degrades T_c. We evaluate the REPME associated with the O-breathing vibration and find it to be almost zero for the $Ba_3Bi_2O_7$ compound ($n = 2$ member), resulting in a very weak EPC and nonsuperconductivity, as is seen in experiments [72]. While general factors may

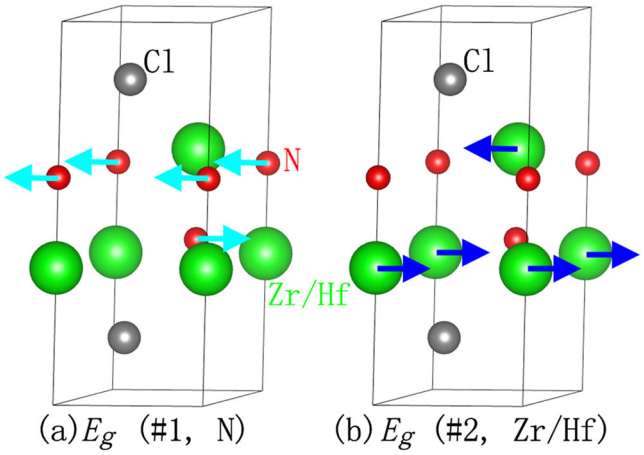

FIG. 5. Simplified crystal structure of ZrNCl/HfNCl. The arrows show (a) the E_g mode with in-plane N vibration and (b) the E_g mode with in-plane Zr/Hf vibration.

promote superconductivity in layered materials relative to their three-dimensional version, a system-specific calculation for the $BaBiO_3$ family reveals that in this family the dominant effect is the reduction of the coupling of the phonon modes to the electrons in the two-dimensional materials, which results in a reduction of T_c.

VI. TRANSITION-METAL CHLORONITRIDES

We turn to another member of the other high-temperature superconductors: the electron-doped MNX (M = Ti, Zr, and Hf; N = nitrogen; X = Cl, Br, and I). These materials are also proximate to an insulating state, and their T_c's are 16.5, 16, and 25.5 K for electron-doped α-TiNCl, β-ZrNCl, and β-HfNCl, respectively [73,74]. A LRT LDA calculation reported λ about 0.52 and $\omega_{\log}$ about 36.4 meV in 1/6 electron-doped ZrNCl [14], which gives T_c only 6 K (assuming $\mu^* = 0.1$) and is insufficient to account for its 16 K superconductivity, raising again the question of what is the mechanism of superconductivity in this family.

A. Crystal structure

ZrNCl (and HfNCl) crystallizes in a rhombohedral structure whose unit cell is built up with three neutral $(ZrNCl)_2$ units in a hexagonal structure. The neutral $(ZrNCl)_2$ units are connected via a weak van der Waals force along the c axis. Since the adjacent layers of the $(ZrNCl)_2$ units are weakly coupled, we ignore the shifting between the layers for simplicity, which results in a hexagonal unit cell (space group $P\bar{3}m1$, number 164; see Fig. 5).

In Fig. 5, we show two E_g vibration modes that involve mainly in-plane vibrations of the nitrogen atoms [Fig. 5(a)] and the Zr/Hf atoms [Fig. 5(b)]. For simplicity, we ignore the small vibrations of the rest atoms in each mode. Such a simplification has negligible influence on the calculated phonon frequencies, as shall be shown in the following subsection.

We include in Table II the structural parameters used in our calculations for ZrNCl, $Li_{0.25}$ZrNCl, HfNCl, and $Na_{0.25}$HfNCl. Note that we simplify the structure to a single layer of the $(Zr/HfNCl)_2$ unit. This simplification is expected to have little impact on the calculated electronic structures and lattice dynamics, due to the weak van der Waals force between the layers.

B. Density of states

The scQPGW, DFT HSE06, and DFT GGA calculated total densities of states for the parent ZrNCl and HfNCl compounds are shown in Fig. 6 and compared to the available experiments reported in Ref. [75]. While the overall shape of the DOS is similar in all the methods, the bandwidths of the valence states and the band gap between the valence states and the conduction states differ substantially. We collect the valence bandwidths and the fundamental band gaps in Table III and compare them to the experimental values reported in Refs. [75,76]. Clearly, the HSE06 accounts very well for the valence bandwidths and band gaps in both materials, whereas the GGA (scQPGW) underestimates (overestimates) the bandwidths by 0.5–0.7 eV (0.3–0.4 eV) and the fundamental band gaps by about 1.0 eV (0.5 eV).

Upon electron doping, except for a shift of the chemical potential (Fermi energy), the overall DOS of $Na_{0.25}$HfNCl remains unchanged, as is shown in Fig. 7(b), which is consistent with the experimental observations reported in Ref. [77]. Here, the HSE06 functional again correctly

TABLE II. The crystal structures of ZrNCl, $Li_{0.25}$ZrNCl, HfNCl, and $Na_{0.25}$HfNCl used in our calculations. The atomic positions are Zr/Hf, [0, 0, z(Zr/Hf)] and [2/3, 1/3, $-z$(Zr/Hf)]; N, [0, 0, z(N)] and [2/3, 1/3, $-z$(N)]; and Cl, [1/3, 2/3, z(Cl)] and [1/3, 2/3, $-z$(Cl)]. Note that in the space group $P\bar{3}m1$, the atomic positions are shifted to Zr/Hf, [2/3, 1/3, z(Zr/Hf)] and [1/3, 2/3, $-z$(Zr/Hf)]; N, [2/3, 1/3, z(N)] and [1/3, 2/3, $-z$(N)]; and Cl, [0, 0, z(Cl)] and [0, 0, $-z$(Cl)]. Here, we stick to the notation for the experimental structure.

Compound	a	c	z(Zr/Hf)	z(N)	z(Cl)	Experiment
ZrNCl	3.6046	9.224	0.3577	0.5931	0.1634	Reference [80]
$Li_{0.25}$ZrNCl	3.591	9.280	0.6379	0.4086	0.1655	Reference [101]
HfNCl	3.5767	9.237	0.3585	0.5928	0.1639	Reference [80]
$Na_{0.25}$HfNCl	3.5879	9.8928	0.6309	0.4110	0.1676	Reference. [102]

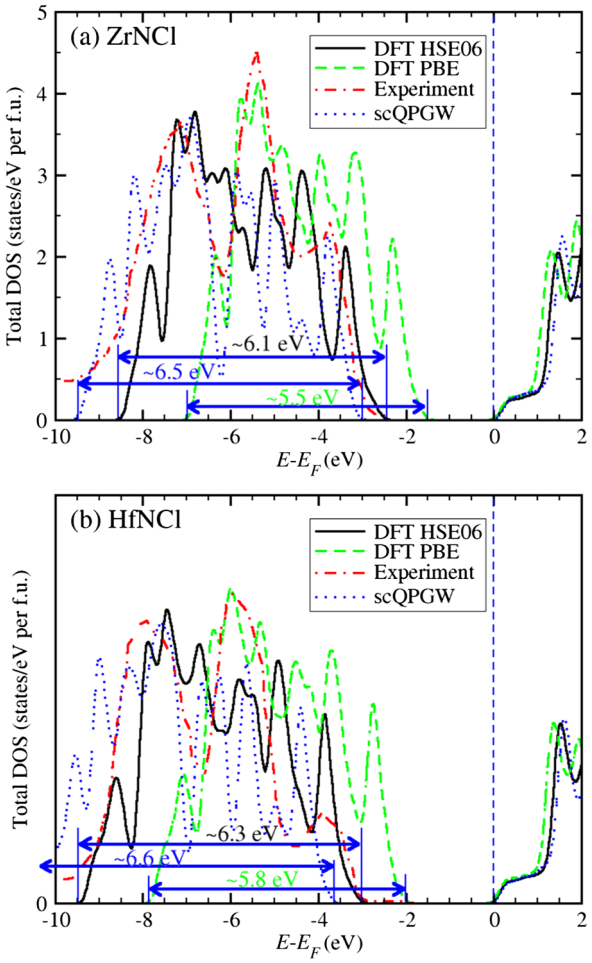

FIG. 6. Density of states of (a) ZrNCl and (b) HfNCl. The theoretical total DOS is calculated using the scQP*GW* method and the PBE functional and the HSE06 hybrid functional within DFT. The experimental data are the photoemission spectra taken from Ref. [75].

reproduces the valence bandwidth and the gap between the valence bands and the conduction bands, whereas the GGA underestimates both quantities to similar magnitudes as in the parent compound. On the other hand, the calculated valence bandwidths in $Li_{0.25}ZrNCl$ increase by about 0.7–0.8 eV, compared to the parent compound ZrNCl, as is shown in Fig. 7(a) and Table III. This observation is consistent with the trend seen in the experiments [76], where the valence bandwidths in $Na_{0.42}ZrNCl$ increase to about 7.0 eV. Note that the HSE06 again gives a better estimation of the valence bandwidth than the GGA in $Li_{0.25}ZrNCl$.

As a result, the electronic structures in both the parent and the electron-doped ZrNCl and HfNCl are much better accounted for by the DFT HSE06 than by the DFT GGA.

C. Phonon frequencies

It was suggested [14] that the in-plane optical phonons (E_g mode) from vibrations of N and Zr atoms dominate the EPC in $Li_{1/6}ZrNCl$. We therefore compute the phonon frequencies at the Γ and K points of two E_g modes involving the in-plane vibration of the N and Zr/Hf atoms, as is shown in Fig. 5 in ZrNCl, $Li_{0.25}ZrNCl$, HfNCl, and $Na_{0.25}HfNCl$ using the frozen-phonon method with both the GGA and HSE06 functionals. The structural parameters used in our calculations are the same as in Table II. We use a $2 \times 2 \times 1$ supercell to calculate the phonon frequencies at the K point. The phonon frequencies in $Li_{0.25}ZrNCl$ ($Na_{0.25}HfNCl$) are calculated using a $2 \times 2 \times 1$ supercell where two Li (Na) atoms are placed at (0, 0, 0) and (0.5, 0.5, 0) in the supercell. The calculated phonon frequencies are shown in Table IV and compared with a previous LRT LDA calculation [14] and a DFT-for-superconductors (SCDFT) calculation with the random phase approximation (RPA) [15] and available experiments [78,79]. A few points can be drawn from our calculations.

(1) The phonon frequencies at the Γ point are similar in the HSE06 and the GGA and are close to experimental values, which is consistent with other theoretical studies [14,15].

(2) Upon electron doping, both E_g phonon modes strongly soften along the Γ-K direction. For the E_g phonon mode involving in-plane nitrogen vibration, the HSE06 (GGA) calculated phonon frequency at the K point softens by 29%/25% (16%/18%) or 21.8/19.3 meV (12.5/13.7 meV), compared to the

TABLE III. The valence bandwidths and the fundamental band gaps in ZrNCl and HfNCl and their electron-doped compounds, calculated using the DFT GGA, DFT HSE06, and scQP*GW* methods and compared with experiments [75–77]. The DFT HSE06 accurately reproduces both the valence bandwidths and the fundamental band gaps in both materials, whereas the DFT GGA underestimates the bandwidth by 0.5–0.7 eV and the band gap by about 1.0 eV. The scQP*GW* overestimates the valence bandwidth by 0.3–0.4 eV and the band gap by 0.5 eV.

	Compounds	DFT GGA	DFT HSE06	scQP*GW*	Experiment
Valence bandwidth	ZrNCl	5.5	6.1	6.5	6.1 (Ref. [75])
	$Li_{0.25}ZrNCl$	6.3	6.8		7.0 (Ref. [76] for $Na_{0.42}ZrNCl$)
	HfNCl	5.8	6.3	6.6	6.3 (Ref. [75])
	$Na_{0.25}HfNCl$	5.8	6.3		6.3 (Ref. [77] for $Na_{0.22}HfNCl$)
Fundamental band gap	ZrNCl	1.6	2.5	3.1	2.5 (Ref. [76])
	HfNCl	2.0	3.1	3.7	3.2–3.4 (Ref. [75])

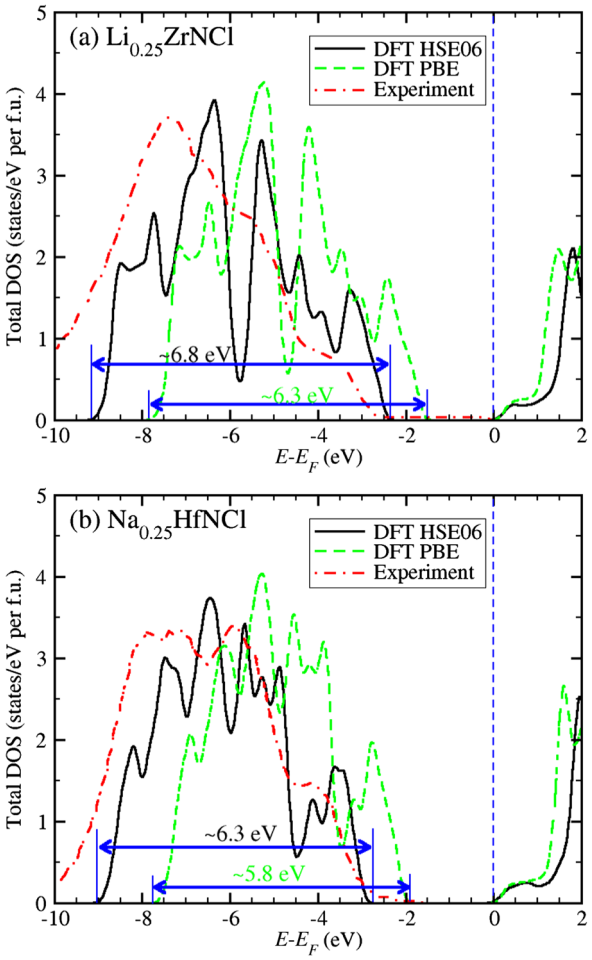

FIG. 7. Density of states of (a) $Li_{0.25}ZrNCl$ and (b) $Na_{0.25}HfNCl$. The theoretical total DOS is calculated using both the PBE functional and the HSE06 hybrid functional. Doping is approximated by placing two Li/Na atoms at (0, 0, 0) and (0.5, 0.5, 0) in the $2 \times 2 \times 1$ supercell. The experimental data are the photoemission spectra taken from Ref. [76] for $Na_{0.42}ZrNCl$ and from Ref. [77] for $Na_{0.22}HfNCl$.

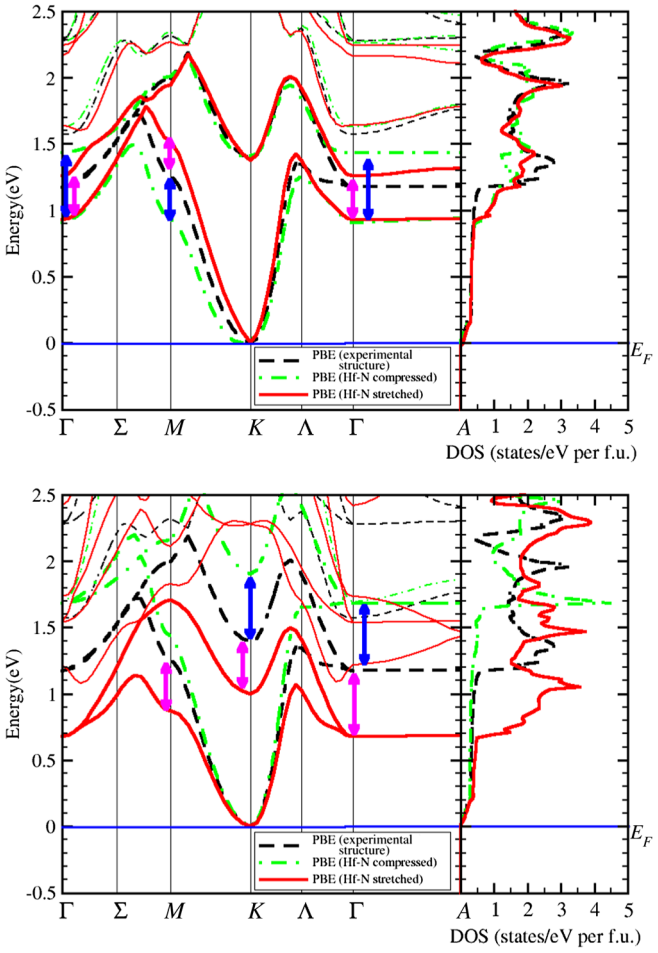

FIG. 8. Band structure and density of states of β-HfNCl. The band structure and density of states of β-HfNCl are calculated using the PBE functional with the experimental crystal structure [80] and with the experimental crystal structure with the Hf and/or N atoms shifted in the ab plane (top panel) and along the c axis (bottom panel) such that the Hf-N bond is compressed or stretched by 0.09 Å. For simplicity, the different layer stacking along the c axis is ignored. Note that the Fermi level is set to the bottom of the conduction band, since we are interested in electron doping.

Γ point in ZrNCl/HfNCl upon 0.25/f.u. electron doping. The corresponding numbers are 40%/19% (13%/17%) or 10.2/3.5 meV (3.4/3.0 meV) for the E_g mode involving the in-plane Zr/Hf vibration.

(3) The observed softening is not due to a change of the crystal structure induced by doping. As is shown in Table V, we calculate the phonon frequencies with the crystal structures of $Li_{0.25}ZrNCl$ and $Na_{0.25}HfNCl$, but without doping the Li/Na atoms, and find that they are similar to the corresponding values in the parent compounds of ZrNCl and HfNCl, respectively; i.e., we do not observe phonon softening at the K point. Hence, the phonon softening is of electronic rather than structural origin.

Therefore, we conclude that for the E_g phonon modes, (1) a strong EPC occurs around the zone-boundary K point but not the zone-center Γ point, consistent with the LRT LDA results reported in Ref. [14], and (2) the HSE06 has a much stronger EPC around the K point than the GGA does. Our results suggest that while the LDA or GGA produces reasonable phonon frequencies near the Γ point, it overestimates the phonon frequencies around the zone boundary. This overestimation of the LDA or GGA is consistent with the comparison of the LRT LDA phonon DOS with the experimental one in Ref. [14] and can be tested by future experiments.

D. Band structure and electron-phonon coupling

The DFT PBE band structure and density of states of β-HfNCl are shown in Fig. 8, which is calculated with its

TABLE IV. Phonon frequencies of the E_g mode at the zone-center Γ point and the zone-boundary K point in the parent ZrNCl and HfNCl compounds and electron-doped $Li_{0.25}ZrNCl$ and $Na_{0.25}HfNCl$ compounds, calculated by frozen-phonon calculations in the DFT GGA and DFT HSE06 framework. For comparison, the corresponding phonon frequencies from the LRT LDA calculation in Ref. [14], the SCDFT RPA calculations in Ref. [15], as well as from two experimental measurements (experiment 1 from Ref. [78] and experiment 2 from Ref. [79]), are also displayed. For electron doping, two Li/Na atoms are placed at (0, 0, 0) and (0.5, 0.5, 0) in the $2 \times 2 \times 1$ supercell of the original unit cell. Notice the strong phonon softening of the N-N E_g mode near the K point upon electron doping. This phonon softening is strongly enhanced in the DFT HSE06 treatment.

Compound	Mode	DFT GGA			DFT HSE06			LRT LDA	SCDFT RPA	Experiment 1	Experiment 2
	E_g	Γ	K	$\delta\omega$	Γ	K	$\delta\omega$	Γ	Γ	Γ	Γ
ZrNCl	N-N	74.3	79.3	5.0	75.5	82.5	7.0	77.0	77.2	75.0	75.1
$Li_{0.25}ZrNCl$	N-N	77.1	69.6	−7.5	76.7	61.9	−14.8	74.4/78.6	74.8	75.5	
ΔΩ	N-N	2.8	−9.7	−12.5	1.2	−20.6	−21.8	−2.6/1.6	−2.4	0.5	
HfNCl	N-N	76.1	81.0	4.9	76.8	82.3	5.5		80.9		78.6
$Na_{0.25}HfNCl$	N-N	74.9	66.1	−8.8	74.9	61.1	−13.8		75.3		76.5
ΔΩ	N-N	−1.2	−14.9	−13.7	−1.9	−21.2	−19.3		−5.6		−2.1
ZrNCl	Zr-Zr	24.9	33.6	8.7	25.4	37.4	12.0	21.2	23.7	22.2	22.8
$Li_{0.25}ZrNCl$	Zr-Zr	25.8	31.1	5.3	25.3	27.1	1.8	21.0/20.5	22.5	22.1	
ΔΩ	Zr-Zr	0.9	−2.5	−3.4	−0.1	−10.3	−10.2	−0.2/ − 0.7	−1.2	−0.1	
HfNCl	Hf-Hf	18.2	24.4	6.2	18.7	25.1	6.4		20.6		19.4
$Na_{0.25}HfNCl$	Hf-Hf	18.2	21.4	3.2	18.5	21.4	2.9		17.1		19.5
ΔΩ	Hf-Hf	0.0	−3.0	−3.0	−0.2	−3.7	−3.5		−3.5		0.1

experimental crystal structure [80] without and with Hf and/or N atoms shifted in the ab plane and along the c axis to change the Hf-N bonding length. In the calculations, the experimental stacking of the layers along the c axis is ignored for simplicity. Note that the study of Ref. [14] used quite small electron doping (1/6); our calculations suggest that at somewhat higher electron doping, the optical vibrations of N and Zr atoms along the c direction are also relevant to EPC. As the arrows indicate in the left panel of Fig. 8, there are large REPMEs for the first two conduction bands, which are very flat along the Γ-A symmetry line, resulting in a high density of states, as is shown in the right panel of Fig. 8. Such a high density of states makes electron doping hardly change the chemical potential in this region.

The study of Ref. [14] suggests that the EPCs are mainly contributed by in-plane optical phonons (E_g mode) from the vibrations of N and Zr atoms, with strong EPC near the zone-boundary K point. We have shown that the experimental electronic structures of both parent and electron-doped ZrNCl and HfNCl are much better reproduced by the HSE06 than by the LDA. We also find that the phonon frequencies of the E_g mode soften more strongly in the HSE06 than in the LDA near the K point, similar to the

TABLE V. Phonon frequencies of the E_g mode at zone-center Γ point and zone-boundary K point in ZrNCl and HfNCl compounds with structures with and without electron doping calculated by frozen-phonon calculations in the DFT GGA and DFT HSE06 framework. Notice that upon electron doping, the changes in the crystal structure do not cause substantial changes in the phonon frequencies. Therefore, the phonon softening shown in Table IV is electronic in origin rather than structural.

Compound	Structure used	Mode E_g	DFT GGA			DFT HSE06		
			Γ	K	$\delta\omega$	Γ	K	$\delta\omega$
ZrNCl	ZrNCl	N-N	74.3	79.3	5.0	75.5	82.5	7.0
	$Li_{0.25}ZrNCl$	N-N	76.7	81.4	4.7	77.5	83.0	5.5
ΔΩ		N-N	2.4	2.1	−0.3	2.0	0.5	−1.5
HfNCl	HfNCl	N-N	76.1	81.0	4.9	76.8	82.3	5.5
	$Na_{0.25}HfNCl$	N-N	75.4	80.5	5.1	75.9	81.6	5.7
ΔΩ		N-N	−0.7	−0.5	0.2	−0.9	−0.7	0.2
ZrNCl	ZrNCl	Zr-Zr	24.9	33.6	8.7	25.4	37.4	12.0
	$Li_{0.25}ZrNCl$	Zr-Zr	26.1	34.6	8.5	26.5	35.4	8.9
ΔΩ		Zr-Zr	1.2	1.0	−0.2	1.1	−2.0	−3.1
HfNCl	HfNCl	Hf-Hf	18.2	24.4	6.2	18.7	25.1	6.4
	$Na_{0.25}HfNCl$	Hf-Hf	18.1	24.3	6.2	18.5	25.0	6.5
ΔΩ		Hf-Hf	−0.1	−0.1	0.0	−0.2	−0.1	0.1

TABLE VI. The REPME D (eV/Å) for the most important vibration mode, the total EPC λ, the average phonon frequency $\omega_{\log}$ (K), and the calculated T_c (K) in the LDA and the HSE06 are displayed with experimental T_c for selected compounds at optimal electron or hole doping. $\omega_{\log}$ in the HSE06 is estimated from the corresponding LRT LDA value, as is described in Sec. IV C. The critical temperatures in the LDA and the HSE06 are obtained from Eq. (9) using $\mu^* = 0.10$. (We concentrate on the dominating effect of λ and ignore the small variations in the values of μ^* in the considered materials, which, in practice, affects the calculated T_c by a few kelvins but does not affect our conclusions.) We approximate the LDA $\omega_{\log}$ for HfNCl to be about 80% of the value for ZrNCl, according to the masses of Hf and Zr and their contributions to the total λ (about 40%, according to Ref. [14]).

Compounds	Mode	D (LDA)	D (HSE)	λ(LDA)	λ (HSE)	$\omega_{\log}$ (LDA)	$\omega_{\log}$(HSE)	T_c(LDA)	T_c (HSE)	T_c (experiment)
$BaBiO_3$	O breathing at R	7.6	13.3	0.33	1.0	550	450	0.6	31	32.0 [1]
$BaPbO_3$	O breathing at R	10.1	11.2	0.58	0.72	500	480	10.3	18	...
$Ba_3Bi_2O_7$	O breathing at R	Approximately 0	Approximately 0	Approximately 0	Approximately 0	...	...	Approximately 0	Approximately 0	<2 [72]
ZrNCl	E_g at Γ (in plane)	2.9–4.0	3.9–4.7	0.52	0.8	422	390	6.0	18	16 [73]
HfNCl	E_g at Γ (in plane)	3.8–4.4	5.1–5.3		1.1	340	310	...	25	25.5 [2]

oxygen-breathing mode near the zone-boundary points in (Ba, K)BiO_3. The stronger softening of the HSE06 E_g phonon frequencies is consistent with the comparison of the experimental and LRT LDA phonon DOS shown in Ref. [14]. It is therefore appropriate to use our approach [Eq. (3)] to estimate the realistic EPC in this family. In the electron-doped β-ZrNCl compound, the REPMEs of the conduction bands associated with Zr-N vibrations in the plane and along the c direction are substantially enhanced from 2.9–4.0 eV/Å in the LDA to 3.9–4.7 eV/Å in the HSE06. The enhanced REPME in the HSE06 results in $\lambda_H \sim 0.8$ and $T_c = 18$ K (see Table VI), in agreement with the experimental value of 16.0 K. Interestingly, the enhanced electron-phonon coupling evaluated by the DFT HSE06 does not lead to a larger specific heat coefficient $\gamma = \frac{2}{3}(1 + \lambda)\pi^2 k_B^2 N(0)$, compared to its DFT LDA value, because the electronic density of states at the Fermi level, i.e., $N(0)$, is reduced in the DFT HSE06 by about 20%, compared to the DFT LDA at the same time.

E. Material and doping dependence of T_c

Our theory explains several counterintuitive experimental observations. It explains naturally the higher T_c in electron-doped β-HfNCl than in electron-doped β-ZrNCl, despite the fact that the Hf atom is substantially heavier than the Zr atom and would therefore be expected to have a lower frequency and lower T_c in a BCS picture. It turns out that the dominant factor governing the T_c is the value of the REPME, which is substantially larger in β-HfNCl than in β-ZrNCl and increases from 3.8–4.4 eV/Å in the LDA to 5.1–5.3 eV/Å in the HSE06. Since β-HfNCl is isostructural to β-ZrNCl, the enhanced REPMEs give $\lambda_H \sim 1.1$ and $T_c = 25$ K for electron-doped β-HfNCl (see Table VI), in good agreement with the experiments. The 16.5 K superconductivity in electron-doped α-TiNCl [74] may also be well accounted for in the same way.

Another mystery in this family is the weak doping dependence of T_c, which is quite different from the trends in other known high-temperature superconductors, including the $BaBiO_3$-based ones, where T_c depends crucially on the doping level. To understand the weak doping dependence of T_c, notice that in this family the conduction band as shown in Fig. 8 has the largest REPMEs, and thus a strong EPC, at about 1.0 eV above the bottom of the conduction band. In the same energy region, this conduction band, being flat in certain parts of the Brillouin zone (along Γ-A, for example), results in a high density of states, which makes the Fermi level hardly change with increasing doping level after some critical doping. The combination of the large REPMEs and the high density of states in the same energy region is likely a plausible explanation of the weak doping dependence of T_c in the HfNCl family.

VII. SUMMARY AND DISCUSSION

A. Summary

Table VI summarizes our results on selected lattice dynamical properties (REPMEs, $\omega_{\log}$), the EPC, and the T_c within the Migdal-Eliashberg theory for the materials studied above. Enhancements of the REPMEs in the more advanced and accurate HSE06 screened-hybrid-functional treatment and the scQPGW method, compared to the LDA, give rise to stronger EPC strengths and the softening of strongly electron-phonon-coupled phonon modes, consistent with many experimental observations, as is discussed

above. The enhanced EPC and renormalized phonon frequency $\omega_{\log}$ readily account for the rather high-temperature superconductivity in the doped bismuthates and transition-metal chloronitrides within the Migdal-Eliashberg theory. In addition, using the important REPMEs, we can explain the material dependence of superconductivity, such as high T_c (up to 32 K) in (Ba, K)BiO_3, intermediate T_c (< 20 K) in (Ba, La)PbO_3 and Ba(Pb, Bi)O_3, and low T_c (< 2 K) in $(Ba, K)_3 \times (Bi, Pb)_2O_7$. We are also able to explain the material and doping dependence of T_c in A_xHfNCl and A_xZrNCl ($A =$ Li, Na, etc.).

B. Two general sources of the underestimation of EPI by LDA

The underestimation of the EPI by the LDA (and GGA; in general, the GGA is omitted for conciseness in the discussion) in materials close to a metal-insulator transition is very general, and is closely related to the failure of the LDA in describing the ground-state properties of the parent compounds. This underestimation can be understood intuitively as follows: The LDA overestimates dielectric screening, while the EPI is inversely proportional to the dielectric constant [81]; therefore, the EPI strength is reduced in LDA relative to its true value.

The materials studied in this paper represent two general sources that cause the underestimation of the EPI by the LDA. The first general source is the underestimation of the relevant bandwidths by the LDA, which causes an underestimation of the REPMEs. The transition-metal chloronitrides represent this case, where the LDA underestimates the bandwidth of the lowest conduction band by about 10% in the parent compounds and 20% in the 1/4 electron-doped compounds, compared to the HSE06 treatment. (See Figs. 6 and 7 for the first peak positions in the DOS of the conduction bands from the GGA, HSE06, and/or scQP*GW*.) The second general source is the underestimation of the fundamental band gap by the LDA, where the fundamental band gap is caused by atomic distortions. In this case, the fundamental band gap is closely connected to the REPMEs of the corresponding atomic distortions. The bismuthates belong to the second case, where the fundamental band gap is of an indirect type and is only about 0.15 eV in the LDA [13], while the experimental value is in the range of 0.5–0.9 eV [82]. Notice that the corresponding value in the HSE06 treatment is about 0.65 eV [41].

C. Screened and unscreened hybrid functionals: HSE06 vs B3LYP

There is much doubt about the applicability of a hybrid functional to metallic materials, partially because the famous Becke-Lee-Yang-Parr hybrid (B3LYP) functional fails in describing metallic systems. One reason is that the B3LYP functional fails to attain the exact homogeneous electron gas limit [40] because of the spin-density wave instability in the Hartree-Fock method [39]. Paier, Marsman, and Kresse found that observing this limit is exceedingly important for extended systems [37,40]. On the other hand, the HSE-type screened functional has been designed to exactly describe the homogeneous electron gas; therefore, the HSE-type functional performs much better than the B3LYP functional [40]. Detailed comparisons of the performances of B3LYP- and HSE-type functionals and other functionals are available in the literature (see, for example, Refs. [40,54]). For lattice dynamical properties, it was found that the B3LYP functional overestimates the EPI of some phonon modes in extended systems such as graphene and graphite [83], whereas in the molecular systems such as C_{60}, both the B3LYP- and HSE-type functionals show similar improved estimations of the EPI [84,85]. Therefore, in the present paper, we choose the screened-hybrid-functional HSE06 to study the doped bismuthates and transition-metal chloronitrides, as they are extended metallic materials. The HSE06 functional is proven to be a good choice, as it reproduces accurately the electronic structures and phonon frequencies of the considered materials.

D. Screening parameter

In the construction of the HSE-type screened hybrid functional, it includes 1/4 of the screened nonlocal exchange potential, whose range is determined by a range-separation parameter μ, where $\mu = 0, 0.2$, and ∞ corresponds to the PBE0, HSE06, and PBE functionals, respectively [54]. In more metallic materials, the HSE06 functional tends to overestimate the bandwidths and might perform worse than the conventional LDA functional [54]. To correct this issue of the HSE06 functional, the range-separation parameter μ in the HSE-type functional has to be adjusted so as to get better agreements with the experimental or QP*GW* electronic structures in the normal state. We note that in the strongly overdoped region of the bismuthates and transition-metal chloronitrides, the overscreening problem of the LDA becomes less severe and the screening parameter in the HSE06 functional has to be adjusted. Since the QP*GW* method can determine the degree of nonlocality of the exchange-correlation potential self-consistently, the μ parameter in the screened hybrid functional can be tuned to fit the QP*GW* results. In this way, the μ parameter in the screened hybrid functional can be determined by the QP*GW* method and is no longer an empirical parameter. Here, we take MgB_2 as an example to demonstrate the determination of the μ parameter. We show below that corrections beyond the LDA or GGA are needed to better describe experimental observations in MgB_2. By adjusting μ in the HSE-type functional to fit the QP*GW* results, a modified HSE functional fixes the discrepancies between the LDA or GGA and experiments, and results in slightly stronger EPC strength and larger phonon linewidths, which are consistent with the fact that

the LDA or GGA functional, on average, underestimates the experimental phonon linewidths [86–89]. Therefore, the modified HSE functional provides a better estimation of the EPC strength in MgB_2.

While the LDA or GGA is commonly considered to be accurate for MgB_2, there are various experimental observations that are not well reproduced by the LDA or GGA. For example, it was shown in Ref. [90] that the LDA or GGA overestimated several de Haas–van Alphen frequencies by 200 T. For the smaller Fermi surface formed by the σ band in the Γ plane, the LDA or GGA overestimated its size by 30% [90]. In the optical conductivity, the peak of the interband transition, experimentally at about 2.6 eV, was estimated to be located at about 2.4 eV by the DFT LDA or GGA [91]. That is to say, the LDA or GGA underestimates the splitting between the lower σ band and the upper π band. These overestimations and underestimations of experimental observations by the LDA or GGA suggest that corrections beyond the LDA or GGA are needed to faithfully reproduce experimental results.

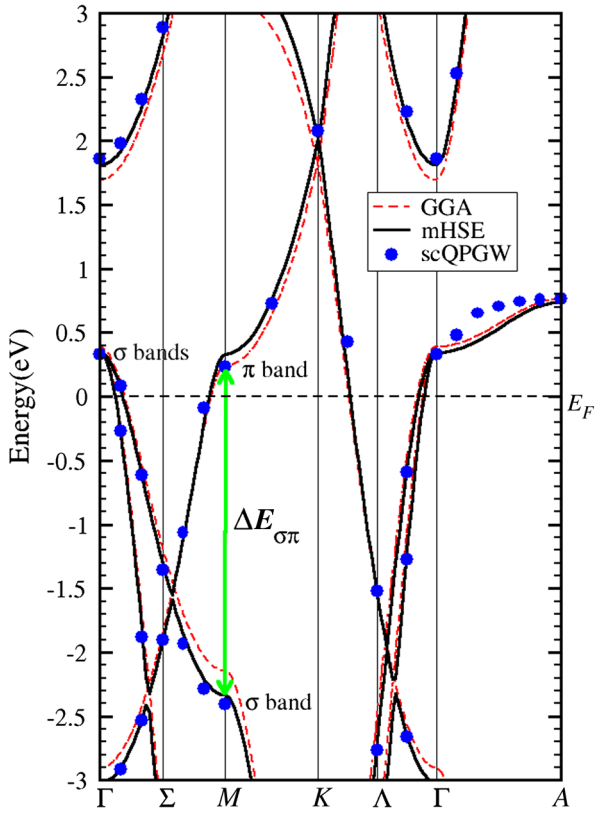

FIG. 9. Band structure of MgB_2, calculated by the DFT GGA, the DFT mHSE06, and the scQPGW. The DFT mHSE ($\mu = 0.6$) band structure agrees well with that calculated by the scQPGW, with a splitting of the π band and σ band at the M point (i.e., $\Delta E_{\sigma\pi}$) about 2.6 eV, in good agreement with experiments [91]. The DFT GGA underestimates this splitting $\Delta E_{\sigma\pi}$ by about 0.2 eV and overestimates the size of the σ Fermi surface centered at the Γ point.

On the other hand, there are unexpectedly large discrepancies in the LDA or GGA results of the same quantity reported by different groups. For example, the de Haas–van Alphen frequencies of the same Fermi surfaces calculated by a few groups differ by 100 to 300 T [90]. As another example, the phonon frequency of the most important E_{2g} mode varies from 470–515 cm^{-1} [92] to 585 cm^{-1} [29] and to 575–665 cm^{-1} [93]. Note the differences in the values of the reported frequencies in the preprint and published versions of Refs. [92,93]. These large discrepancies in the reported LDA or GGA results indicate unusual sensitivity to the calculational details in MgB_2.

In the following, we correct the above discrepancies between the LDA or GGA and experiments in the optical conductivity and de Haas–van Alphen frequencies by using a HSE-type screened hybrid functional and the QPGW method. The range of the nonlocal exchange in the HSE-type functional is adjusted by tuning the μ parameter to fit the scQPGW results, such as band structure (shown in Fig. 9) and DOS (shown in Fig. 10). In the calculations, we use the experimental structure (lattice constants $a = 3.0834$ Å and $c = 3.5213$ Å, space group $P6/mmm$, number 191) from Ref. [94].

In Table VII, we collect a few quantities, calculated by the DFT GGA, the DFT HSE06, the DFT mHSE (a modified HSE functional with $\mu = 0.6$), and the scQPGW, and compare them with experimental values and previous theoretical calculations. The included quantities are the splitting $\Delta E_{\sigma\pi}$ between the lower σ band and the π band

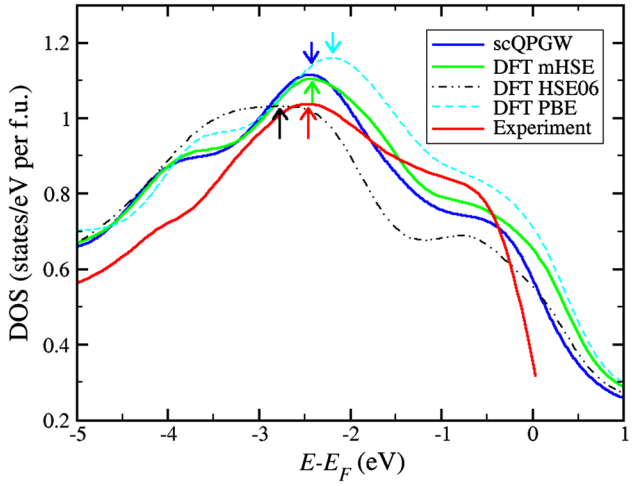

FIG. 10. Density of states of MgB_2 calculated by the scQPGW, the DFT mHSE, the DFT HSE06, and the DFT GGA and compared to experiments [109]. For each DOS of all the data, an arrow is drawn to indicate the peak position, which is mainly contributed by the B $2p$ states. The DOS of the scQPGW method, the DFT mHSE ($\mu = 0.6$), and experiments [109] share a common peak at about -2.4 eV, whereas the DFT GGA underestimates this peak position by 0.2 eV (at about -2.2 eV) and the DFT HSE06 overestimates it by 0.4 eV (at about -2.8 eV).

TABLE VII. Various quantities in MgB_2 calculated by the DFT GGA, DFT HSE06, DFT mHSE ($\mu = 0.6$), and scQP*GW*, and compared to available experiments, including the first interband transition peak position (in eV) in optics, the de Haas–van Alphen frequency (in T) from the Fermi surface formed by the lower σ band in the Γ plane, the phonon frequency (in meV) of the E_{2g} mode, and the calculated reduced electron-phonon matrix electron (in eV/Å) of the E_{2g} mode.

	DFT GGA $\mu = \infty$	DFT HSE06 $\mu = 0.2$	DFT mHSE $\mu = 0.6$	scQP*GW*	Experiment	Other DFT LDA or GGA
Peak position $\Delta E_{\sigma\pi}$ (eV)	2.4	3.0	**2.6**	2.6	**2.6** (Ref. [91])	2.4 (Ref. [103])
de Haas–van Alphen frequency $F_{\sigma\Gamma}$ (T)	730	350	**580**		**535–546** (Ref. [90])	728–878 (Refs. [104–106])
Phonon frequency $\omega_{E_{2g}}$ (meV)	71.8	66.0	**70.5**		**69.6–71.2** (Ref. [107])	58–83 (Refs. [29,92,93])
REPME of the E_{2g} mode (eV/Å)	12.3	16.5	13.9			13 (Ref. [108])

around the *M* point (marked as an arrow in Fig. 9), showing as a interband transition peak in the optical conductivity, the de Haas–van Alphen frequency $F_{\sigma\Gamma}$ of the lower σ band in the Γ plane, the phonon frequency $\omega_{E_{2g}}$ of the E_{2g} mode, and the REPME (in eV/Å) of the E_{2g} mode.

Figure 9 shows the band structure of MgB_2 calculated by the DFT GGA, the DFT mHSE ($\mu = 0.6$), and the scQP*GW*. Consistent with the previous LDA or GGA calculations, which are shown in Table VII, our DFT GGA calculation also underestimates the splitting $\Delta E_{\sigma\pi}$ by 0.2 eV and overestimates the de Haas–van Alphen frequency $F_{\sigma\Gamma}$ by 190 T. On the contrary, the DFT HSE06 overestimates $\Delta E_{\sigma\pi}$ by 0.4 eV and underestimates $F_{\sigma\Gamma}$ by 190 T, suggesting that the HSE06 overcompensates for the overscreening of the LDA or GGA. Therefore, we increase μ to reduce the range of the nonlocal exchange potential in the HSE06 functional. We find that a modified HSE-type functional with $\mu = 0.6$ simultaneously fits well to the scQP*GW* results and reproduces the experimental $\Delta E_{\sigma\pi}$, $F_{\sigma\Gamma}$, and $\omega_{E_{2g}}$, as is shown in Table VII and Figs. 9 and 10. As a result, MgB_2 is a material that sits between conventional metals, which are well described by the LDA or GGA functional and conventional insulators, which are much better described by the HSE06 screened hybrid functional.

Since MgB_2 is better described by the mHSE functional with $\mu = 0.6$, we now proceed to estimate the EPC strength in MgB_2, combining the LRT LDA λ and the frozen-phonon calculations. According to Ref. [29], the total LRT LDA λ is about 0.87, of which $\lambda_\sigma = 0.62$ is contributed by the E_{2g} mode of the σ band and $\lambda_\pi = 0.25$ comes from the π band. Here, we renormalize λ_σ and ignore the difference in λ_π because the π band makes a much smaller contribution to the total EPC. The estimated EPC strength in the mHSE functional is $\lambda_{\mathrm{mHSE}} = (13.9/12.3)^2\lambda_\sigma + \lambda_\pi = 0.79 + 0.25 = 1.04$, which is 0.17 bigger than the LRT LDA value. This slightly enhanced λ is consistent with the fact that the LDA or GGA functional, on average, underestimates the experimental phonon linewidths [86–89] and suggests that the mHSE functional provides a better estimation of the EPC strength in MgB_2.

In short, MgB_2 is closer to a conventional superconductor than the bismuthates and transition-metal chloronitrides. Applying the methodology we advocate in this paper, namely, using a screened hybrid functional and/or *GW* method that describes well the normal-state properties to obtain an improved description of the superconducting state, does not lead to dramatic modifications of the existing picture for MgB_2.

Although the difference between the LDA or GGA and the mHSE in MgB_2 is substantially smaller than in the case of (Ba, K)BiO_3, it is a consistent manifestation of the overscreening problem of the LDA or GGA functional. It testifies to our idea that because of the overscreening problem, the LDA or GGA underestimates the EPC in these compounds. The realistic EPC thus has to be evaluated with a method that describes well the experimental electronic structures and phonon frequencies. In addition to the computationally more demanding *GW* method, the HSE06 screened hybrid functional within DFT can serve as such a method for (Ba, K)BiO_3 and electron-doped ZrNCl and HfNCl, while a modified HSE-type screened hybrid functional within DFT is suitable for MgB_2.

E. Other materials

There is a class of materials where corrections beyond the LDA or GGA are needed to account for the lattice dynamical properties and EPI. In addition to the doped bismuthates and transition-metal chloronitrides, it was noted that in graphene [83] and organic molecular compounds, such as A_3C_{60} [84,85] and picene [95], *GW* or (screened) hybrid DFT methods are needed to evaluate phonon-related quantities. The latter two have narrow bands and may be in an antiadiabatic regime [96]. This class may include other puzzling materials, such as Tl_xPbTe [97] and undoubtedly many other systems still to be discovered.

F. Recent progress

Recently, the theory presented in this article has been confirmed from several directions. The optical conductivities computed with the *ab initio* parameters derived in this article are in good agreement with experimental measurements in (Ba, K)BiO_3 [98]. A new family of mixed-valent materials in the class of the other high-temperature superconductors $ATlX_3$, where A = Cs, Rb, and K and X = F, Cl, and Br, such as $CsTlCl_3$ and $CsTlF_3$, has been rationally designed in theory [99] and successfully synthesized in the experimental laboratory [100].

VIII. CONCLUSIONS

In conclusion, we show in this paper that first-principles calculations based on the LDA or GGA functional can significantly underestimate the EPI strength in certain materials, where there are large nonlocal correlations such as materials in the vicinity of a metal-insulator transition. The doped $BaBiO_3$ and HfNCl family are such materials—the parent compounds are insulators, while the sufficiently doped compounds are metals. This underestimation of the EPI is caused by the overscreening of the LDA or GGA in insulators, semiconductors, and low-carrier bad metals, which results in an underestimation of the relevant bandwidths and/or the fundamental band gaps—two general sources of the underestimation of electron-phonon coupling.

We present a simple but efficient method to evaluate the realistic EPC in these materials by combining the LDA or GGA linear-response calculations and a few supercell calculations, using a more advanced and accurate method such as *GW* and screened-hybrid-functional DFT that is able to provide a significantly improved description of normal-state electronic structures and lattice dynamical properties of the materials, in comparison to LDA or GGA.

We apply our method to evaluate the EPC in the doped $BaBiO_3$ and HfNCl family and find that the realistic electron-phonon couplings are significantly enhanced over the LDA values and are strong enough to account for the rather high-temperature superconductivity in these materials within the Migdal-Eliashberg theory. The puzzling discrepancies between theory and experiments in these materials are naturally resolved with our method. The other high-temperature superconductors, such as those summarized in Refs. [4,5], are thus strongly coupled superconductors where the coupling of the electrons to the lattice vibrations requires the treatment of correlations beyond the LDA or GGA.

Our method is also important for the rational design of new superconductors and other EPI-related functional materials through first-principles calculations because reliably determining the electron-phonon coupling is an essential step. As an example, we predict up to 18 K superconductivity in the perovskite $Ba_{1-x}La_xPbO_3$ compound around $x = 0.7$.

Our work suggests that a critical reexamination of the realistic EPC is necessary in these and other materials, such as the correlated cuprates and iron-based superconductors. Even in MgB_2, as discussed above, a careful reexamination shows that the LDA slightly underestimates the EPC.

Finally, we reiterate that our approach of estimating the realistic EPC can be improved by including more phonon modes and that our work calls for implementing the linear-response technique into *GW* and screened-hybrid-functional DFT to achieve a more accurate evaluation of the realistic EPC.

ACKNOWLEDGMENTS

We are grateful to Mac Beasley and Bob Cava for renewing our interest in this problem, and to Sergey Savrasov, Warren Pickett, and Kristjan Haule for their useful comments. This work was supported by the AFOSR-MURI Program.

[1] R. J. Cava, B. Batlogg, J. J. Krajewski, R. Farrow, L. W. Rupp, Jr., A. E. White, K. Short, W. F. Peck, and T. Kometani, *Superconductivity near 30 K without Copper: The* $Ba_{0.6}K_{0.4}BiO_3$ *Perovskite*, Nature (London) **332**, 814 (1988).

[2] S. Yamanaka, K.-I. Hotehama, and H. Kawaji, *Superconductivity at 25.5 K in Electron-Doped Layered Hafnium Nitride*, Nature (London) **392**, 580 (1998).

[3] O. Gunnarsson, *Superconductivity in Fullerides*, Rev. Mod. Phys. **69**, 575 (1997).

[4] W. E. Pickett, *The Other High-Temperature Superconductors*, Physica (Amsterdam) **296B**, 112 (2001).

[5] W. E. Pickett, *The Next Breakthrough in Phonon-Mediated Superconductivity*, Physica (Amsterdam) **468C**, 126 (2008).

[6] A. Taraphder, H. R. Krishnamurthy, R. Pandit, and T. V. Ramakrishnan, *Negative-U Extended Hubbard Model for Doped Barium Bismuthates*, Phys. Rev. B **52**, 1368 (1995).

[7] C. M. Varma, *Missing Valence States, Diamagnetic Insulators, and Superconductors*, Phys. Rev. Lett. **61**, 2713 (1988).

[8] W. Jin, M. H. Degani, R. K. Kalia, and P. Vashishta, *Superconductivity in* $Ba_{1-x}K_xBiO_3$, Phys. Rev. B **45**, 5535 (1992).

[9] T. M. Rice and L. Sneddon, *Real-Space and* $\vec{k}$*-Space Electron Pairing in* $BaPb_{1-x}Bi_xO_3$, Phys. Rev. Lett. **47**, 689 (1981).

[10] G. Vielsack and W. Weber, *Search for Negative U in the* $Ba_{1-x}K_xBi_{1-y}Pb_yO_3$ *System Using Constrained Density-Functional Theory*, Phys. Rev. B **54**, 6614 (1996).

[11] W. A. Harrison, *Valence-Skipping Compounds as Positive-U Electronic Systems*, Phys. Rev. B **74**, 245128 (2006).

[12] S. Y. Savrasov, *Linear-Response Theory and Lattice Dynamics: A Muffin-Tin-Orbital Approach*, Phys. Rev. B **54**, 16470 (1996).

[13] V. Meregalli and S. Y. Savrasov, *Electron-Phonon Coupling and Properties of Doped* $BaBiO_3$, Phys. Rev. B **57**, 14453 (1998).

[14] R. Heid and K.-P. Bohnen, *Ab Initio Lattice Dynamics and Electron-Phonon Coupling in* Li_xZrNCl, Phys. Rev. B **72**, 134527 (2005).

[15] R. Akashi, K. Nakamura, R. Arita, and M. Imada, *High-Temperature Superconductivity in Layered Nitrides* β-Li_xMNCl (M = Ti, Zr, Hf)*: Insights from Density Functional Theory for Superconductors*, Phys. Rev. B **86**, 054513 (2012).

[16] W. E. Pickett, R. E. Cohen, and H. Krakauer, *Lattice Instabilities, Isotope Effect, and High-*T_c *Superconductivity in* $La_{2-x}Ba_xCuO_4$, Phys. Rev. Lett. **67**, 228 (1991).

[17] H. Krakauer, W. E. Pickett, and R. E. Cohen, *Large Calculated Electron-Phonon Interactions in* $La_{2-x}M_xCuO_4$, Phys. Rev. B **47**, 1002 (1993).

[18] A. Lanzara *et al.*, *Evidence for Ubiquitous Strong Electron-Phonon Coupling in High-Temperature Superconductors*, Nature (London) **412**, 510 (2001).

[19] T. Cuk, D. H. Lu, X. J. Zhou, Z.-X. Shen, T. P. Devereaux, and N. Nagaosa, *A Review of Electron-Phonon Coupling Seen in the High-*T_c *Superconductors by Angle-Resolved Photoemission Studies (ARPES)*, Phys. Status Solidi B **242**, 11 (2005).

[20] O. Gunnarsson, and O. Rösch, *Interplay between Electron-Phonon and Coulomb Interactions in Cuprates*, J. Phys. Condens. Matter **20**, 043201 (2008).

[21] S. M. Shapiro, G. Shirane, and J. D. Axe, *Measurements of the Electron-Phonon Interaction in* Nb *by Inelastic Neutron Scattering*, Phys. Rev. B **12**, 4899 (1975).

[22] M. G. Mitch, S. J. Chase, and J. S. Lannin, *Raman Scattering and Electron-Phonon Coupling in* Rb_xC_{60}, Phys. Rev. Lett. **68**, 883 (1992).

[23] E. L. Wolf, J. Zasadzinski, G. B. Arnold, D. F. Moore, J. M. Rowell, and M. R. Beasley, *Tunneling and the Electron-Phonon-Coupled Superconductivity of* Nb_3Sn, Phys. Rev. B **22**, 1214 (1980).

[24] O. Gunnarsson, H. Handschuh, P. S. Bechthold, B. Kessler, G. Ganteför, and W. Eberhardt, *Photoemission Spectra of* C_{60}^-*: Electron-Phonon Coupling, Jahn-Teller Effect, and Superconductivity in the Fullerides*, Phys. Rev. Lett. **74**, 1875 (1995).

[25] K. Prassides, C. Christides, M. J. Rosseinsky, J. Tomkinson, D. W. Murphy, and R. C. Haddon, *Neutron Spectroscopy and Electron-Phonon Coupling in Alkali-Metal-Doped Fullerides*, Europhys. Lett. **19**, 629 (1992).

[26] D. Kasinathan, J. Kuneš, A. Lazicki, H. Rosner, C. S. Yoo, R. T. Scalettar, and W. E. Pickett, *Superconductivity and Lattice Instability in Compressed Lithium from Fermi Surface Hot Spots*, Phys. Rev. Lett. **96**, 047004 (2006).

[27] Z. P. Yin, S. Y. Savrasov, and W. E. Pickett, *Linear Response Study of Strong Electron-Phonon Coupling in Yttrium under Pressure*, Phys. Rev. B **74**, 094519 (2006).

[28] Z. P. Yin, F. Gygi, and W. E. Pickett, *Competing Phases, Strong Electron-Phonon Interaction, and Superconductivity in Elemental Calcium under High Pressure*, Phys. Rev. B **80**, 184515 (2009).

[29] Y. Kong, O. V. Dolgov, O. Jepsen, and O. K. Andersen, *Electron-Phonon Interaction in the Normal and Superconducting States of* MgB_2, Phys. Rev. B **64**, 020501(R) (2001).

[30] N. Tralshawala, J. F. Zasadzinski, L. Coffey, W. Gai, M. Romalis, Q. Huang, R. Vaglio, and K. E. Gray, *Tunneling,* $\alpha^2F(\omega)$*, and Transport in Superconductors:* Nb, V, VN, $Ba_{1-x}K_xBiO_3$, *and* $Nd_{1.85}Ce_{0.15}CuO_4$, Phys. Rev. B **51**, 3812 (1995).

[31] M. A. Green, K. Prassides, D. A. Neumann, and P. Day, *Lattice Dynamics of Semiconducting, Metallic, and Superconducting* $Ba_{1-x}K_xBiO_3$ *Studied by Inelastic Neutron Scattering*, Chem. Mater. **7**, 888 (1995).

[32] H. Khosroabadi, J. Kobayashi, K. Tanaka, S. Miyasaka, S. Tajima, H. Uchiyama, and A. Q. R. Baron, *Softening of Bond Stretching Phonon Mode in* $Ba_{1-x}K_xBiO_3$ *Superconductor*, J. Supercond. Novel Magn. **23**, 1385 (2010).

[33] H. Khosroabadi, S. Miyasaka, J. Kobayashi, K. Tanaka, H. Uchiyama, A. Q. R. Baron, and S. Tajima, *Softening of Bond-Stretching Phonon Mode in* $Ba_{1-x}K_xBiO_3$ *at the Metal-Insulator Transition*, Phys. Rev. B **83**, 224525 (2011).

[34] A. J. Cohen, P. Mori-Sánchez, and W. T. Yang, *Insights into Current Limitations of Density Functional Theory*, Science **321**, 792 (2008).

[35] A. Georges, G. Kotliar, W. Krauth, and M. J. Rozenberg, *Dynamical Mean-Field Theory of Strongly Correlated Fermion Systems and the Limit of Infinite Dimensions*, Rev. Mod. Phys. **68**, 13 (1996).

[36] G. Kotliar, S. Y. Savrasov, K. Haule, V. S. Oudovenko, O. Parcollet, and C. A. Marianetti, *Electronic Structure Calculations with Dynamical Mean-Field Theory*, Rev. Mod. Phys. **78**, 865 (2006).

[37] T. M. Henderson, J. Paier, and G. E. Scuseria, *Accurate Treatment of Solids with the HSE Screened Hybrid*, Phys. Status Solidi B **248**, 767 (2011).

[38] A. V. Krukau, O. A. Vydrov, A. F. Izmaylov, and G. E. Scuseria, *Influence of the Exchange Screening Parameter on the Performance of Screened Hybrid Functionals*, J. Chem. Phys. **125**, 224106 (2006).

[39] A. W. Overhauser, *Spin Density Waves in an Electron Gas*, Phys. Rev. **128**, 1437 (1962).

[40] J. Paier, M. Marsman, and G. Kresse, *Why Does the B3LYP Hybrid Functional Fail for Metals?*, J. Chem. Phys. **127**, 024103 (2007).

[41] C. Franchini, G. Kresse, and R. Podloucky, *Polaronic Hole Trapping in Doped* $BaBiO_3$, Phys. Rev. Lett. **102**, 256402 (2009).

[42] C. Franchini, A. Sanna, M. Marsman, and G. Kresse, *Structural, Vibrational, and Quasiparticle Properties of the Peierls Semiconductor* $BaBiO_3$*: A Hybrid Functional and Self-Consistent* $GW + Vertex$*-Corrections Study*, Phys. Rev. B **81**, 085213 (2010).

[43] P. Sun and G. Kotliar, *Extended Dynamical Mean-Field Theory and GW Method*, Phys. Rev. B **66**, 085120 (2002).

[44] S. Biermann, F. Aryasetiawan, and A. Georges, *First-Principles Approach to the Electronic Structure of Strongly Correlated Systems: Combining the GW Approximation and Dynamical Mean-Field Theory*, Phys. Rev. Lett. **90**, 086402 (2003).

[45] D. Jacob, K. Haule, and G. Kotliar, *Combining the Hybrid Functional Method with Dynamical Mean-Field Theory*, Europhys. Lett. **84**, 57009 (2008).

[46] X. Dai, S. Y. Savrasov, G. Kotliar, A. Migliori, H. Ledbetter, and E. Abrahams, *Calculated Phonon Spectra of Plutonium at High Temperatures*, Science **300**, 953 (2003).

[47] S. Y. Savrasov and G. Kotliar, *Linear Response Calculations of Lattice Dynamics in Strongly Correlated Systems*, Phys. Rev. Lett. **90**, 056401 (2003).

[48] O. Rösch and O. Gunnarsson, *Electron-Phonon Interaction in the t-J Model*, Phys. Rev. Lett. **92**, 146403 (2004) and references therein.

[49] K. Hummer, J. Harl, and G. Kresse, *Heyd-Scuseria-Ernzerhof Hybrid Functional for Calculating the Lattice Dynamics of Semiconductors*, Phys. Rev. B **80**, 115205 (2009).

[50] J. Wróbel, K. J. Kurzydłowski, K. Hummer, G. Kresse, and J. Piechota, *Calculations of* ZnO *Properties Using the Heyd-Scuseria-Ernzerhof Screened Hybrid Density Functional*, Phys. Rev. B **80**, 155124 (2009).

[51] L. Qin, Y. Duan, H. Shi, L. Shi, and G. Tang, *Hybrid Density Functional Theory Studies of AlN and GaN under Uniaxial Strain*, J. Phys. Condens. Matter **25**, 045801 (2013).

[52] J. Graciani, A. M. Márquez, J. J. Plata, Y. Ortega, N. C. Hernández, A. Meyer, C. M. Zicovich-Wilson, and J. F. Sanz, *Comparative Study on the Performance of Hybrid DFT Functionals in Highly Correlated Oxides: The Case of* CeO_2 *and* Ce_2O_3, J. Chem. Theory Comput. **7**, 56 (2011).

[53] Y. Okamoto, M. Saito, and A. Oshiyama, *Hybrid Density-Functional Study of the Vibrational Frequency of a* H_2 *Molecule at the Tetrahedral Site of Silicon*, Phys. Rev. B **58**, 7701 (1998).

[54] M. Marsman, J. Paier, A. Stroppa, and G. Kresse, *Hybrid Functionals Applied to Extended Systems*, J. Phys. Condens. Matter **20**, 064201 (2008).

[55] P. B. Allen, *Neutron Spectroscopy of Superconductors*, Phys. Rev. B **6**, 2577 (1972).

[56] G. Kresse and J. Furthmüller, *Efficiency of Ab-Initio Total Energy Calculations for Metals and Semiconductors Using a Plane-Wave Basis Set*, Comput. Mater. Sci. **6**, 15 (1996).

[57] J. P. Perdew, K. Burke, and M. Ernzerhof, *Generalized Gradient Approximation Made Simple*, Phys. Rev. Lett. **77**, 3865 (1996).

[58] P. Blaha, K. Schwarz, G. K. H. Madsen, D. Kvasnicka, and J. Luitz, *WIEN2K: An Augmented Plane Wave + Local Orbitals Program for Calculating Crystal Properties* (Vienna University of Technology, Vienna, Austria, 2001).

[59] S. Y. Savrasov and D. Y. Savrasov, *Electron-Phonon Interactions and Related Physical Properties of Metals from Linear-Response Theory*, Phys. Rev. B **54**, 16487 (1996).

[60] D. E. Cox and A. W. Sleight, *Mixed-Valent* $Ba_2Bi^{3+}Bi^{5+}O_6$*: Structure and Properties vs Temperature*, Acta Crystallogr. Sect. B **35**, 1 (1979).

[61] W. T. Fu, D. Visser, and D. J. W. IJdo, *High-Resolution Neutron Powder Diffraction Study on the Structure of* $BaPbO_3$, Solid State Commun. **134**, 647 (2005).

[62] C.-K. Loong, P. Vashishta, R. K. Kalia, W. Jin, M. H. Degani, D. G. Hinks, D. L. Price, J. D. Jorgensen, B. Dabrowski, A. W. Mitchell, D. R. Richards, and Y. Zheng, *Phonon Density of States and Oxygen-Isotope Effect in* $Ba_{1-x}K_xBiO_3$, Phys. Rev. B **45**, 8052 (1992).

[63] K.-H. Lee, K. J. Chang, and M. L. Cohen, *First-Principles Calculations of the Coulomb Pseudopotential* μ^**: Application to Al*, Phys. Rev. B **52**, 1425 (1995).

[64] A. L. Kutepov and S. G. Kutepova, *The Ab Initio Ground State Properties and Magnetic Structure of Plutonium*, J. Phys. Condens. Matter **15**, 2607 (2003).

[65] A. Kutepov, S. Y. Savrasov, and G. Kotliar, *Ground-State Properties of Simple Elements from GW Calculations*, Phys. Rev. B **80**, 041103(R) (2009).

[66] L. F. Mattheiss and D. R. Hamann, *Electronic Structure of* $BaPb_{1-x}Bi_xO_3$, Phys. Rev. B **28**, 4227 (1983).

[67] M. Shirai, N. Suzuki, and K. Motizuki, *Electron-Lattice Interaction and Superconductivity in* $BaPb_{1-x}Bi_xO_3$ *and* $Ba_xK_{1-x}BiO_3$, J. Phys. Condens. Matter **2**, 3553 (1990).

[68] H. Namatame, A. Fujimori, H. Torii, T. Uchida, Y. Nagata, and J. Akimitsu, *Effects of Hole Doping and Electron-Phonon Interaction on the Electronic Structure of* $Ba_{1-x}K_xBiO_3$ *Studied by Photoemission Spectroscopy*, Phys. Rev. B **50**, 13674 (1994).

[69] M. Braden, W. Reichardt, A. S. Ivanov, and A. Yu. Rumiantsev, *Anamolous Dispersion of LO Phonon Branches in* $Ba_{0.6}K_{0.4}BiO_3$, Europhys. Lett. **34**, 531 (1996).

[70] A. P. Menushenkov, A. V. Tsvyashchenko, D. V. Eremenko, K. V. Klementev, A. V. Kuznetsov, V. N. Trofimov, and L. N. Fomichev, *Superconductivity in the* $Ba_{1-x}La_xPbO_3$ *System*, Phys. Solid State **43**, 613 (2001).

[71] P. Monthoux and G. G. Lonzarich, *Magnetically Mediated Superconductivity: Crossover from Cubic to Tetragonal Lattice*, Phys. Rev. B **66**, 224504 (2002).

[72] R. J. Cava, T. Siegrist, W. F. Peck, Jr., J. J. Krajewski, B. Batlogg, and J. Rosamilia, $(Ba, K)_3Bi_2O_7$*: A Layered Bismuth Oxide*, Phys. Rev. B **44**, 9746 (1991).

[73] S. Yamanaka, *High-*T_c *Superconductivity in Electron-Doped Layer Structured Nitrides*, Annu. Rev. Mater. Sci. **30**, 53 (2000).

[74] S. Yamanaka, T. Yasunaga, K. Yamaguchi, and M. Tagawa, *Structure and Superconductivity of the Intercalation Compounds of TiNCl with Pyridine and Alkali Metals as Intercalants*, J. Mater. Chem. **19**, 2573 (2009).

[75] A. Ino, K. Yamazaki, T. Yamasaki, M. Higashiguchi, K. Shimada, H. Namatame, M. Taniguchi, T. Oguchi, X. Chen, and S. Yamanaka, *Angle-Resolved-Photoemission Study of Layer-Structured Nitride* β*-HfNCl*, J. Electron Spectrosc. Relat. Phenom. **144**, 667 (2005).

[76] T. Yokoya, T. Takeuchi, S. Tsuda, T. Kiss, T. Higuchi, S. Shin, K. Iizawa, S. Shamoto, T. Kajitani, and T. Takahashi, *Valence-Band Photoemission Study of* β*-ZrNCl and the Quasi-Two-Dimensional Superconductor* Na_xZrNCl, Phys. Rev. B **70**, 193103 (2004).

[77] T. Yokoya, Y. Ishiwata, S. Shin, S. Shamoto, K. Iizawa, T. Kajitani, I. Hase, and T. Takahashi, *Changes of Electronic Structure across the Insulator-to-Metal Transition of Quasi-Two-Dimensional Na-Intercalated* β*-HfNCl Studied by Photoemission and X-Ray Absorption*, Phys. Rev. B **64**, 153107 (2001).

[78] P. Adelmann, B. Renker, H. Schober, M. Braden, and F. Fernandez-Diaz, *Lattice Dynamics of Li-ZrNCl: An Electron Doped Layered Superconductor*, J. Low Temp. Phys. **117**, 449 (1999).

[79] A. Cros, A. Cantarero, D. Beltrán-Porter, J. Oró-Solé, and A. Fuertes, *Lattice Dynamics of Superconducting Zirconium and Hafnium Nitride Halides*, Phys. Rev. B **67**, 104502 (2003).

[80] X.-A. Chen, T. Koiwasaki, and S. Yamanaka, *High-Pressure Synthesis and Crystal Structures of β-MNCl (M = Zr and Hf)*, J. Solid State Chem. **159**, 80 (2001).

[81] P. B. Allen and B. Mitrovic, in *Solid State Physics* (Academic, New York, 1982), Vol. 37, p. 1–92.

[82] H. Namatame, A. Fujimori, H. Takagi, S. Uchida, F. M. F. de Groot, and J. C. Fuggle, *Electronic Structure and the Metal-Semiconductor Transition in* $BaPb_{1-x}Bi_xO_3$ *Studied by Photoemission and X-Ray-Absorption Spectroscopy*, Phys. Rev. B **48**, 16917 (1993).

[83] M. Lazzeri, C. Attaccalite, L. Wirtz, and F. Mauri, *Impact of the Electron-Electron Correlation on Phonon Dispersion: Failure of LDA and GGA DFT Functionals in Graphene and Graphite*, Phys. Rev. B **78**, 081406(R) (2008).

[84] C. Faber, J. L. Janssen, M. Côté, E. Runge, and X. Blase, *Electron-Phonon Coupling in the* C_{60} *Fullerene within the Many-Body GW Approach*, Phys. Rev. B **84**, 155104 (2011).

[85] J. L. Janssen, M. Côté, S. G. Louie, and M. L. Cohen, *Electron-Phonon Coupling in* C_{60} *Using Hybrid Functionals*, Phys. Rev. B **81**, 073106 (2010).

[86] A. Shukla, M. Calandra, M. d'Astuto, M. Lazzeri, F. Mauri, C. Bellin, M. Krisch, J. Karpinski, S. M. Kazakov, J. Jun, D. Daghero, and K. Parlinski, *Phonon Dispersion and Lifetimes in* MgB_2, Phys. Rev. Lett. **90**, 095506 (2003).

[87] A. Q. R. Baron, H. Uchiyama, Y. Tanaka, S. Tsutsui, D. Ishikawa, S. Lee, R. Heid, K.-P. Bohnen, S. Tajima, and T. Ishikawa, *Kohn Anomaly in* MgB_2 *by Inelastic X-Ray Scattering*, Phys. Rev. Lett. **92**, 197004 (2004).

[88] A. Q. R. Baron, H. Uchiyama, R. Heid, K. P. Bohnen, Y. Tanaka, S. Tsutsui, D. Ishikawa, S. Lee, and S. Tajima, *Two-Phonon Contributions to the Inelastic X-Ray Scattering Spectra of* MgB_2, Phys. Rev. B **75**, 020505(R) (2007).

[89] M. d'Astuto, M. Calandra, S. Reich, A. Shukla, M. Lazzeri, F. Mauri, J. Karpinski, N. D. Zhigadlo, A. Bossak, and M. Krisch, *Weak Anharmonic Effects in* MgB_2*: A Comparative Inelastic X-Ray Scattering and Raman Study*, Phys. Rev. B **75**, 174508 (2007).

[90] J. R. Cooper, A. Carrington, P. J. Meeson, E. A. Yelland, N. E. Hussey, L. Balicas, S. Tajima, S. Lee, S. M. Kazakov, and J. Karpinski, *de Haas–van Alphen Effect in* MgB_2 *Crystals*, Physica (Amsterdam) **385C**, 75 (2003).

[91] V. Guritanu, A. B. Kuzmenko, D. van der Marel, S. M. Kazakov, N. D. Zhigadlo, and J. Karpinski, *Anisotropic Optical Conductivity and Two Colors of* MgB_2, Phys. Rev. B **73**, 104509 (2006).

[92] J. Kortus, I. I. Mazin, K. D. Belashchenko, V. P. Antropov, and L. L. Boyer, *Superconductivity of Metallic Boron in* MgB_2, Phys. Rev. Lett. **86**, 4656 (2001); arXiv:cond-mat/0101446.

[93] G. Satta, G. Profeta, F. Bernardini, A. Continenza, and S. Massidda, *Electronic and Structural Properties of Superconducting* MgB_2, $CaSi_2$, *and Related Compounds*, Phys. Rev. B **64**, 104507 (2001); *Electronic and Structural Properties of Superconducting Diborides and Calcium Disilicide in the* AlB_2 *Structure*, arXiv:cond-mat/0102358.

[94] M. E. Jones and R. E. Marsh, *The Preparation and Structure of Magnesium Boride,* MgB_2, J. Am. Chem. Soc. **76**, 1434 (1954).

[95] G. Giovannetti and M. Capone, *Electronic Correlation Effects in Superconducting Picene from Ab Initio Calculations*, Phys. Rev. B **83**, 134508 (2011).

[96] M. Capone, M. Fabrizio, C. Castellani, and E. Tosatti, *Colloquium: Modeling the Unconventional Superconducting Properties of Expanded* A_3C_{60} *Fullerides*, Rev. Mod. Phys. **81**, 943 (2009).

[97] Y. Matsushita, H. Bluhm, T. H. Geballe, and I. R. Fisher, *Evidence for Charge Kondo Effect in Superconducting* Tl*-Doped* PbTe, Phys. Rev. Lett. **94**, 157002 (2005).

[98] R. Nourafkan, F. Marsiglio, and G. Kotliar, *Model of the Electron-Phonon Interaction and Optical Conductivity of* $Ba_{1-x}K_xBiO_3$ *Superconductors*, Phys. Rev. Lett. **109**, 017001 (2012).

[99] Z. P. Yin and G. Kotliar, *Rational Material Design of Mixed-Valent High-*T_c *Superconductors*, Europhys. Lett. **101**, 27002 (2013).

[100] M. Retuerto, T. Emge, J. Hadermann, P. W. Stephens, M. R. Li, Z. P. Yin, M. Croft, A. Ignatov, S. J. Zhang, Z. Yuan, C. Jin, J. W. Simonson, M. C. Aronson, A. Pan, D. N. Basov, G. Kotliar, and M. Greenblatt, Synthesis and Properties of Charge-Ordered Thallium Halide Perovskites: $CsTl^{1+}_{0.5}Tl^{3+}_{0.5}X_3$ (X = F, Cl)—Theoretical Precursors for Superconductivity? (to be published).

[101] X.-A. Chen, L.-P. Zhu, and S. Yamanaka, *The First Single-Crystal X-Ray Structural Refinement of the Superconducting Phase* $Li_{0.2(1)}ZrNCl$ *Derived by Intercalation*, J. Solid State Chem. **169**, 149 (2002).

[102] J. Oró-Solé, C. Frontera, B. Martínez, D. Beltrán-Porter, M. R. Palacín, and A. Fuertes, *A New Intermediate Intercalate in Superconducting Sodium-Doped Hafnium Nitride Chloride*, Chem. Commun. (Cambridge) 26 (2005) 3352.

[103] A. B. Kuz'menko, F. P. Mena, H. J. A. Molegraaf, D. van der Marel, B. Gorshunov, M. Dressel, I. I. Mazin, J. Kortus, O. V. Dolgov, T. Muranaka, and J. Akimitsu, *Manifestation of Multiband Optical Properties of* MgB_2, Solid State Commun. **121**, 479 (2002).

[104] I. I. Mazin and J. Kortus, *Interpretation of the de Haas–van Alphen Experiments in* MgB_2, Phys. Rev. B **65**, 180510(R) (2002).

[105] H. Rosner, J. M. An, W. E. Pickett, and S.-L. Drechsler, *Fermi Surfaces of Diborides:* MgB_2 *and* ZrB_2, Phys. Rev. B **66**, 024521 (2002).

[106] H. Harima, *Energy Band Structures of* MgB_2 *and Related Compounds*, Physica (Amsterdam) **378C**, 18 (2002).

[107] W. X. Li, Y. Li, R. H. Chen, R. Zeng, M. Y. Zhu, H. M. Jin, and S. X. Dou, *Electron-Phonon Coupling Properties in* MgB_2 *Observed by Raman Scattering*, J. Phys. Condens. Matter **20**, 255235 (2008).

[108] J. M. An and W. E. Pickett, *Superconductivity of* MgB_2*: Covalent Bonds Driven Metallic*, Phys. Rev. Lett. **86**, 4366 (2001).

[109] T. A. Callcott, L. Lin, G. T. Woods, G. P. Zhang, J. R. Thompson, M. Paranthaman, and D. L. Ederer, *Soft-X-Ray Spectroscopy Measurements of the p-like Density of States of* B *in* MgB_2 *and Evidence for Surface Boron Oxides on Exposed Surfaces*, Phys. Rev. B **64**, 132504 (2001).